Research paper

Cold thermal energy storage for industrial CO_2 refrigeration systems using phase change material: An experimental study

Håkon Selvnes [a,*], Yosr Allouche [a], Armin Hafner [a], Christian Schlemminger [b], Ignat Tolstorebrov [a]

[a] *Norwegian University of Science and Technology, Department of Energy and Process Engineering, Kolbjørn Hejes vei 1B, NO-7491, Trondheim, Norway*
[b] *Sintef Energy Research, Kolbjørn Hejes vei 1D, NO-7465, Trondheim, Norway*

ARTICLE INFO

ABSTRACT

Refrigeration systems in industrial food processing plants are large users of electric energy and often show high peak power consumption. Cold thermal energy storage (CTES) technology integrated into refrigeration systems can reduce the peak power requirement and achieve peak shifting by decoupling the supply and demand of the refrigeration load. This paper presents the design and performance of a CTES unit consisting of a pillow plate heat exchanger (PP-HEX) immersed into a low-temperature phase change material (PCM) as the storage medium. It is one of the first experimental investigations featuring a large-scale technical solution that allows for coupling the evaporation and condensation processes of the refrigeration system with the melting and solidification of a low-temperature PCM in the same heat exchanger. The charging and discharging performance of the plates-in-tank CTES unit was extensively tested using CO_2 as the refrigerant and a commercial PCM with phase change temperature of -9.6 °C. The charging time was found to be mainly affected by the refrigerant evaporation temperature, while the discharging rate and discharged energy over the cycle was higher when increasing the refrigerant condensing temperature. Using a plate pitch of 30 mm resulted in the highest mean discharge rate and total discharged energy over the cycle with 9.79 kW and 17.04 kWh, respectively. The flexible CTES-PCM unit can be adapted to fit several refrigeration load characteristics and temperature levels by changing the PP-HEX geometry and type of PCM used as the storage medium.

1. Introduction

Refrigeration demands in industrial food processing plants can vary significantly over a day or week, depending on the production schedules. As a result, the electric power consumption of such plants is characterised by peaks and valleys. Cold thermal energy storage (CTES) technology has received increased interest for the past two decades from researchers and stakeholders in the refrigeration sector as a measure to reduce the peaks in the cooling load that occurs in many refrigeration systems, e.g. in food processing plants and air-conditioning systems. Furthermore, CTES technology plays an important role to provide higher flexibility and enabling demand-side management in refrigeration systems [1]. In addition to CTES applications in air-conditioning [2] and domestic refrigeration [3], the current research on CTES applications focuses on the different links in the food cold chain, such as food transport and packaging, commercial and supermarket refrigeration systems, and industrial food processing plants [4]. More research on CTES technology has been identified as an important factor for further market penetration of environment-friendly CO_2 supermarket refrigeration systems across the world [5]. CTES technology

using a phase change material (PCM) as the storage medium is of particular interest due to the high volumetric energy storage capacity of latent heat storage (LHS) systems compared to sensible heat storage (SHS) systems [6]. PCMs are materials that utilise the phase transition between the solid and liquid state for storing energy. As an example, Allouche et al. [7] showed that using an LHS with microencapsulated PCM slurry for CTES application for implementation into an air-conditioning system provided a storage capacity enhancement of up to 53% compared to using the equivalent volume of water as the SHS medium. PCMs can be divided into two main categories, organic PCMs and inorganic PCMs [8]. The two most studied groups of PCMs for CTES applications are paraffins (organic PCM, primarily consisting of mixtures of alkanes) and eutectic salt-water solutions (inorganic PCM), which have become readily available commercially the last ten years [4,6,9]. Eutectic salt-water solutions are mixtures of different salt hydrates and water with high volumetric storage capacity compared to most organic PCMs due to the high density and latent heat capacity of these PCMs. The thermal conductivity of eutectic water-salt solutions is also considerably higher than for most organic PCMs, comparable

---

Nomenclature

Abbreviations

ACC	Auxiliary CO_2 circuit
$CTES$	Cold thermal energy storage
GHC	Glycol heating circuit
HEX	Heat exchanger
PCC	Primary CO_2 circuit
PCM	Phase change material
PID	Process and instrumentation diagram
PP	Pillow plate
SCC	Secondary CO_2 circuit

Symbols

$\dot{E}$	Energy flow
$\dot{m}$	Mass flow rate
b	Thickness
d	Diameter
E	Energy
h	Enthalpy
L	Length
n	Number
s	Welding spot pitch
T	Temperature
t	Time
W	Width

Greek letters

δ	Height, distance
η	Apparent viscosity
γ	Shear rate
ρ	Density

Subscripts

C	Charging
CO_2	Carbondioxide
$cond$	Condensation
D	Discharging
$evap$	Evaporation
fus	Fusion
g	Glycol
L	Longitudinal
o	Outer
PCM	Phase change material
PP	Pillow plate
s	Solid
sat	Saturation
SP	Welding spot
T	Transversal
th	Theoretical
w	Wall

to the thermal conductivity of water (approximately 0.6 W/(m K)). However, some significant drawbacks of these PCMs are their high rate of supercooling, incongruent melting, and being corrosive to certain metals [10]. Paraffins are substances that consist of chains of saturated hydrocarbons that can be produced from either fossil or bio-based sources [11], where the latter is offered by a few producers such as

PureTemp LLC [12] and Croda International Plc [13]. Producing PCM from non-edible plant oils or waste cooking oil instead of fossil sources could be a measure to increase the sustainability of TES technology, and organic PCMs in particular [14]. Paraffins have some favourable properties when used as an LHS medium, such as not being corrosive to metals, low supercooling, stable and non-reactive behaviour and no phase segregation issues [15]. The most important drawback of PCMs in general, and organic PCM in particular, is the low thermal conductivity of these materials, limiting the heat transfer rate when used in a CTES system. Extensive research has been carried out to enhance the conductivity of various PCMs by adding highly conductive inserts such as metal particles, carbon materials and metal foams [16,17], but the cost of these enhanced materials remains a limitation for widespread implementation.

When considering the integration of PCM heat exchanger (PCM-HEX) units into a refrigeration system, Selvnes et al. [4] proposed a classification into two groups; CTES units integrated into the secondary refrigerant circuit and CTES units integrated into the primary refrigeration circuit. In the first group, the PCM-HEX is integrated into the secondary refrigeration circuit (glycol/water/brine) using a PCM/single-phase fluid heat exchanger (HEX) design. In the second group, the PCM-HEX unit is designed to be integrated directly into the primary refrigerant circuit, employing a PCM/two-phase fluid HEX design. For this design, the CTES unit will act as an evaporator during the charging process and it operates as a condenser for the refrigeration system during the discharging process. Most experimental research on CTES units to date has focused on CTES units integrated into the secondary refrigeration circuit, likely because of the focus on CTES applied to air-conditioning systems in the past, where secondary refrigerant circuits are common. Furthermore, integrating the CTES unit into the primary refrigerant circuit involves much stricter requirements of the CTES unit in terms of often increased refrigerant charge and the pressure class of the equipment, governed by relevant standards such as the European Standard EN-378 and the EU Pressure Equipment Directive (PED) [18]. On the other hand, integration of the CTES unit into the primary refrigerant circuit allows for raising the evaporation temperature during the charging process, increasing the system efficiency compared to using a secondary refrigerant circuit [19].

Demonstration of performance of heat exchanger (HEX) units using PCM as the storage medium is vital to increase the confidence in this CTES technology by manufacturers and stakeholders in the refrigeration industry. Thorough experimental characterisation of promising PCM-HEX units at a laboratory scale is a measure that can contribute to establishing up-scaled pilot plants and demonstration sites in the refrigeration industry, increasing the market penetration of CTES technology. The coil-in-tank, tube-in-tank and plate-in-tank designs are the most frequently investigated PCM-HEX configurations to date. The coil-in-tank and tube-in-tank constitute the major share of past studies. This is probably due to the relatively simple design, simple construction and low cost of these PCM-HEX units for testing at a laboratory scale, particularly when using a single-phase refrigerant inside the pipes. Experimental investigations on the three CTES unit design have been carried out using various storage media including water/ice [20–26], inorganic PCMs [21,27] and organic PCMs [7,28–33]. Furthermore, several manufacturers of CTES systems also use the coil-in-tank design for their commercial products, e.g. the systems from Calmac [34] and Viessmann [35] for thermal energy storage purposes in supermarket refrigeration systems.

Abhishek et al. [24] investigated a coil-in-tank PCM-HEX using water as the PCM and a brine as secondary refrigerant. A study on the effect on the charging and discharging performance by vertical and horizontal tube orientation, tube outlet location and tube size was performed, showing that a vertical tube orientation was generally preferable with up to about 30% improvement for the discharging process. Ballot-Miguet et al. [36] reported the performance of a 500 kWh-capacity ice-on-coil CTES unit integrated into a glycol circuit for
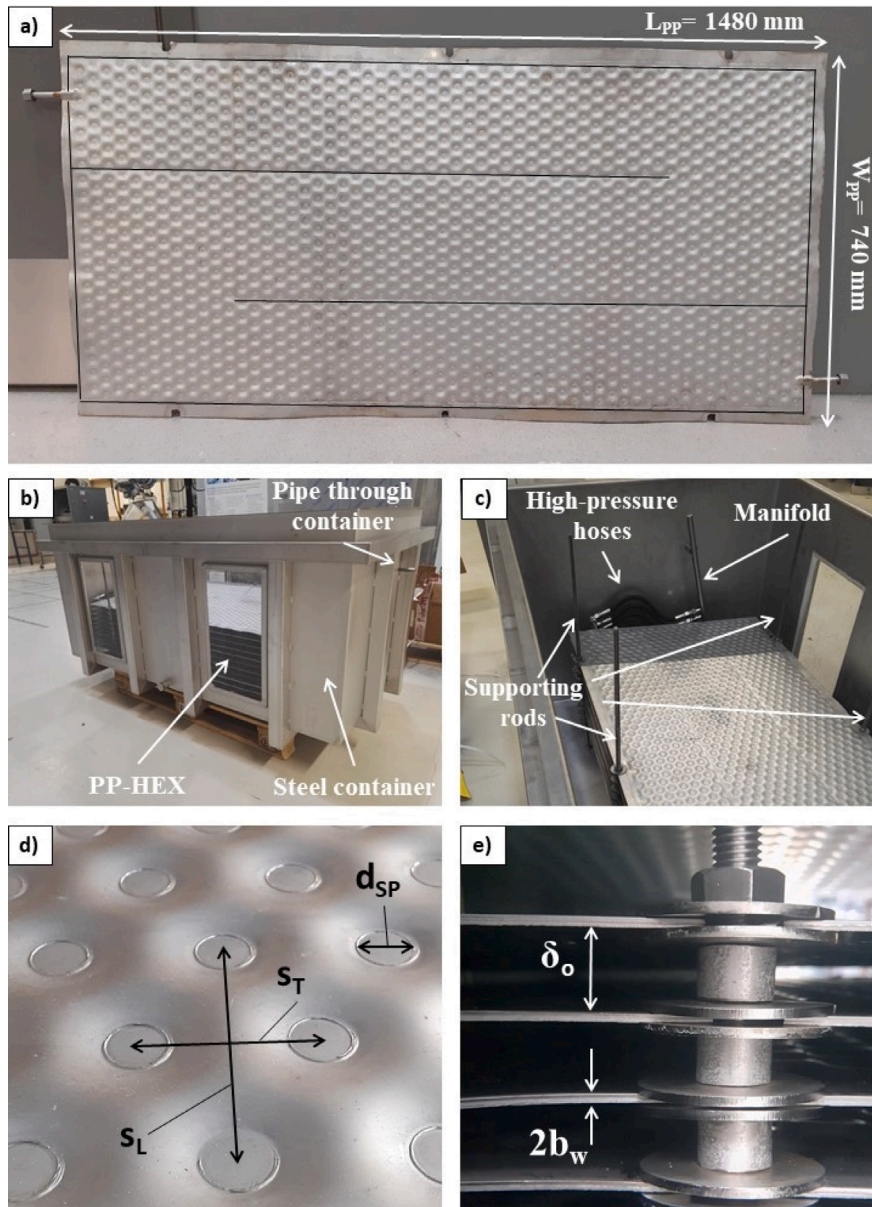
Fig. 1. Overview of the novel CTES unit showing the details of (a) one PP for CO_2 refrigeration with inlet/outlet pipes and the seam welds marked with black lines (b) the CTES unit before assembly in the test facility (c) view of the PP-HEX inside the container (d) the wavy PP surface characteristic with the welding pattern parameters (e) the PP-HEX stack in the CTES unit with vertical plate pitch. Figure first presented in [26].

medium temperature cooling purposes in a supermarket CO_2 refrigeration system. The CTES unit was installed in a supermarket in France and operated as a subcooler for the refrigeration system during high ambient temperatures to improve its performance, reducing the annual electricity consumption by 6%. A plates-in-tank PCM-HEX unit using hexadecane (18 °C) as the PCM, targeted for load shifting purposes in data centres and server rooms was presented by Saeed et al. [32]. The modular PCM-HEX unit was experimentally tested under various conditions, and the unit demonstrated an effectiveness of over 80 % with a mean discharge rate of 4.8 kW. Verpe et al. [37] proposed and numerically investigated the integration of a shell and tube PCM-HEX into a CO_2 refrigeration system for a plate freezer on a fishing vessel. Using dry ice (solid CO_2) as the PCM for storing the cold energy lower than −40 °C, a reduction in the freezing time of the fish by 3.2% was calculated. Qu et al. [31] proposed using a fin-and-tube PCM-HEX (PCM RT10, melting temperature 9.4 °C) to solve the issue of defrosting of the evaporator in a cascade air-source heat pump. The PCM-HEX acted as the heat source for both the high-temperature

circuit (providing heat to condenser) and the low-temperature circuit (for hot gas defrost) in the heat pump during the defrosting process. The experimental results show that the PCM-HEX unit was able to supply a mean discharge rate of 5.09 kW for the defrosting period of about 9 min. Korth et al. [33] experimentally investigated the use of a tube-in-tank PCM-HEX unit as a subcooler to increase the refrigeration capacity of an air conditioning system. The PCM-HEX unit was utilising the direct PCM/refrigerant heat exchange principle and an organic PCM with a melting temperature of 18 °C. An 18% capacity increase of the refrigeration system was demonstrated during the discharge of the PCM-HEX.

The design of a novel modular CTES unit based on the plates-in-tank principle intended for peak shaving of refrigeration load was first presented by Selvnes et al. [38]. The PCM-HEX unit was designed for integration into pump-circulated CO_2 circuits found in many industrial refrigeration systems and large chiller applications. The initial experimental test results and proof of concept were presented by Selvnes

et al. [25] using water/ice as the storage medium, making the PCM-HEX unit suitable for process cooling and air conditioning purposes. The CO_2 was evaporating/condensing inside the plates, while the PCM was freezing/melting on the surface of the plates during the charging and discharging processes, respectively. The work was continued by an extensive investigation of various HEX configurations and a variation of the refrigerant parameters, still using water/ice as the PCM [26]. It was shown that the evaporation and condensation temperature of the CO_2 were the most influencing parameters for the charging and discharging cycles, respectively. For the HEX configuration resulting in the largest storage capacity, the mean discharge rate was found to be 7.90 kW over a cycle time of 4.5 h. From the reviewed literature, it is clear that experimental research on PCM-HEX units covering the temperature range below 0 °C to date is very limited, a temperature area of high importance for refrigeration systems in the food cold chain. It is estimated that 40% of all food products need refrigeration [39], while refrigeration is estimated to account for up to 15% of electricity consumption worldwide [40]. More research on low-temperature PCM-HEX units suitable for large-scale installations in refrigeration plants is therefore of key importance to improve energy efficiency, provide flexibility and achieve peak shifting in this sector.

In the current paper, the plates-in-tank PCM-HEX unit presented in earlier studies using water/ice as the PCM [25,26,38] is modified to fit the application of industrial refrigeration plants, specifically for integration into the pump-circulated CO_2 circuit used in CO_2/NH_3 cascade refrigeration systems. To adapt to the temperature requirement of the food processing industry, the available commercial PCMs on the market was mapped and an organic PCM with a melting point of −9.6 °C was selected as the storage medium in the PCM-HEX. First, a presentation of the CTES unit and the experimental setup is given, followed by a description of the experimental procedure for the charging and discharging cycles. Second, the thermo-physical properties of the commercial PCM are characterised, presented and discussed. Finally, the results from the extensive experimental campaign are presented and discussed separately for the charging and discharging processes. The overall performance of the novel PCM-HEX unit is reported and recommendations for future studies are given.

2. Experimental setup

2.1. Cold thermal energy storage unit

The novel CTES unit is presented in Fig. 1b. The design of the unit follows the plates-in-tank principle, and it is composed of a stack of HEX plates placed into a welded stainless steel container filled with an organic PCM (see Fig. 1c). The container is supported on the outside by a frame of square steel tube (see Fig. 1b). It has been shown that stainless steel is the most suitable material for CTES units using PCMs, even for salt hydrate mixtures [41]. The use of a container of polymer materials to hold the PP-HEX and the PCM is generally less expensive, but these were found to be not compatible with certain paraffin PCMs in a long term perspective [29]. The container is filled with PCM to ensure the complete immersion of the PP-HEX into the storage medium. The container is fitted with a lid to prevent the evaporation of the PCM as well as two 1 cm thick windows of acrylic plexiglass on each side to observe the melting and solidification process (see Fig. 1b). The container is insulated with 50 mm polystyrene plates to limit the heat transfer loss from the storage unit to the environment. The HEX consists of a set of plates called pillow plates (PP) due to their characteristic pillow-like surface. These novel type of HEX plates has gained increased attention in both research and the industry due to their compact design and ability to operate under high pressures. Literature on this novel PP-HEX design as well as its performance has been limited compared to other conventional HEX types, e.g. brazed plate HEX or shell and tube HEX. However, several important studies on PP-HEX have been published in the last seven years. For more details

on the main characteristics of the PP geometry, the reader is directed to Piper et al. [42]. To date, most research on PP-HEX has been carried out using a single-phase flow of cooling water inside the PPs [43–47]. The literature on two-phase heat transfer inside the PP remains very limited. To the authors best knowledge, Tran et al. [43] is the only study considering two-phase heat transfer inside the PP channel, where the two-phase heat transfer coefficient of refrigerant R134a was experimentally determined using both natural and forced circulation flows.

Fig. 1a shows one PP used in the PP-HEX for this study. The PP consists of two thin stainless steel metal sheets that are spot-welded together in a particular repetitive pattern by a laser-welding machine. The welding spots form a defined channel where the refrigerant flows and exchange heat with the PCM. The two metal plates are seam-welded along the edges to ensure the sealing of the PP. One pipe is welded to the PP at each end, serving as the inlet and outlet of the refrigerant. Furthermore, two longitudinal seam welds are performed on the plate, as indicated in Fig. 1a. These seam welds generate three flow passes for the refrigerant to flow between the inlet and outlet pipe. This technique is used to direct the refrigerant flow and ensure a better distribution of refrigerant through the PP channels. After the welding process, the PP is inflated by a hydroforming process, applying high water pressure to the inside of the plate. The hydroforming process creates the flow channels for the refrigerant inside the PP and the pillow-like surface characteristic (see Fig. 1d). Any number of PP can then be stacked together to form a complete PP-HEX. The geometrical design parameters of a PP are as follows (see Fig. 1d and e): the spot weld diameter (d_{SP}), the transversal spot weld pitch (s_T), the longitudinal spot weld pitch (s_L), the channel maximum inflation height (δ_i) and the PP wall thickness (b_w). In the current study, a longitudinal welding spot pattern was selected to define the flow channels in the PP, using a longitudinal welding spot pitch of 50 mm and a transversal welding spot pitch of 30 mm. The welding spot arrangement results in a triangular configuration commonly found in the PP industry. The staggered spot-weld pattern of the PP can be seen in Fig. 1d, allowing for heat transfer enhancement between the refrigerant and the storage medium by promoting mixing of the flow inside the PP channel [44]. Important design parameters of PP-HEX are the overall PP length (L_{PP}), the width (W_{PP}), the maximum vertical distance between each PP (δ_o) and the number of plates (n_{PP}), see Fig. 1a and e. The PP-HEX is mounted on a frame of square stainless steel tube for convenient removal and refitting of the stack into the container. The PP-HEX is mounted to the frame by six metal supporting rods, three along each side of the PPs as shown in Fig. 1c. The vertical distance between each PP (plate pitch) in the stack can be selected by using different lengths of cylindrical spacers and washers on the metal rods (see Fig. 1e). The plate pitch is an important parameter because it directly determines the storage capacity of the CTES unit. In this study, the experimental characterisation of the CTES unit was carried out for a plate pitch of 15 mm and 30 mm. Ten PPs were used in the PP-HEX in both plate pitch configurations, resulting in a total heat transfer area of 21.90 m^2. The pipes welded to each end of the PPs are connected to a manifold by high-pressure braided hoses at their respective ends of the PP-HEX. The CTES unit is connected to the experimental test facility by a tube from the manifold that passes through the container wall as shown in Fig. 1a. Approximately 460 kg of liquid PCM was required to completely immerse the PP-HEX for a plate pitch of 30 mm. To handle the expansion of the PCM transitioning between the solid and liquid states, a clearance volume between the container wall and the PP-HEX is included. From the initial testing, the clearance volume (about 10 cm) ensures there is always liquid towards the wall. The thermal expansion of the PCM is then handled through an elevated liquid height in the container, which has atmospheric air above the PCM liquid level. This effectively limits the mechanical stress on both the PP-HEX and the container. The selected geometrical parameters of the PPs and PP-HEX are given in Table 1.
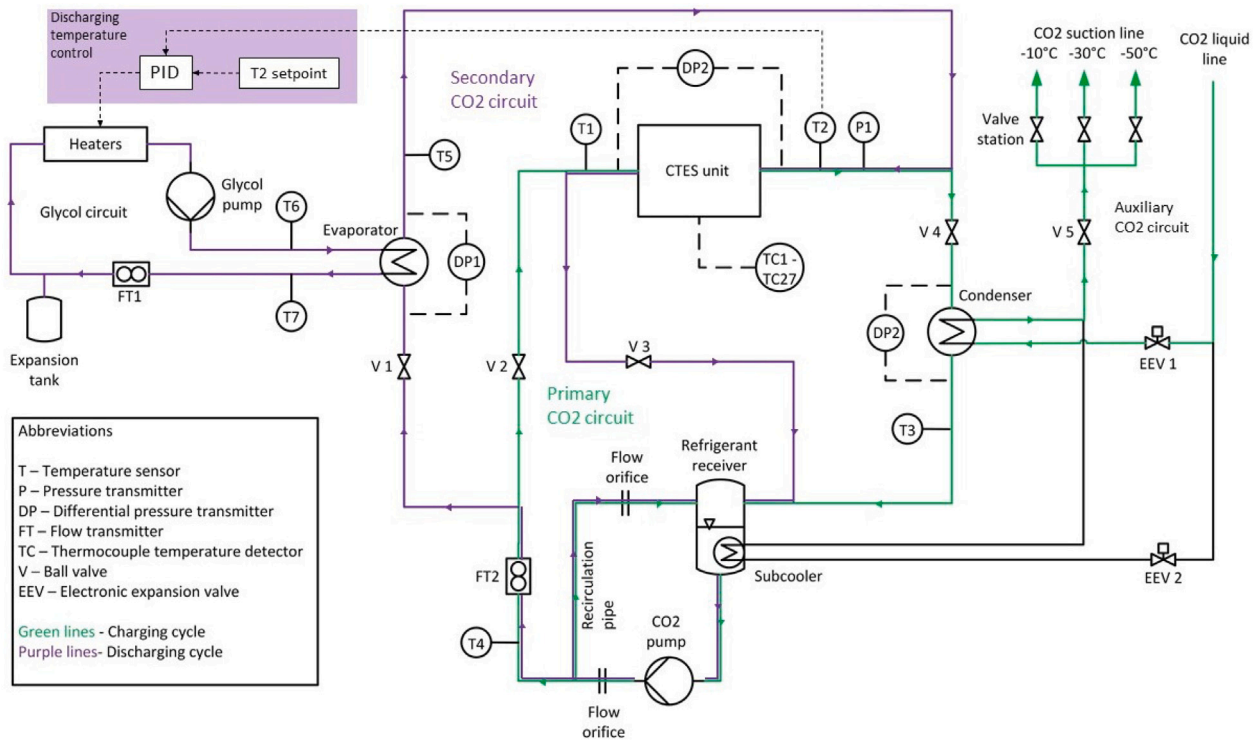
Fig. 2. Piping and instrumentation diagram (PID) of the test facility. Figure first presented in [26].

Table 1
Main geometrical parameters of the PPs and PP-HEX in the novel CTES unit.

Parameter	Value
s_L	50 mm
s_T	30 mm
d_{SP}	10 mm
δ_i	4.3 mm
b_w	1.0 mm
L_{PP}	1480 mm
W_{PP}	740 mm
δ_o	15/30 mm
n_{PP}	10

2.2. Experimental test facility

The experimental test facility was designed by the authors and constructed to test the performance of the CTES unit, previously described in Selvnes et al. [26]. A piping and instrumentation diagram (P&ID) of the test facility is shown in Fig. 2. The facility enables the operator to set and monitor the operating parameters of the refrigerant (e.g. temperature, pressure and flow rate) at the inlet of the CTES unit during both the charging and discharging processes. The test facility can be operated in two different modes: Charging mode (indicated with green lines in Fig. 2) and discharging mode (indicated with purple lines in Fig. 2). Four circuits can be identified in the facility: The primary CO_2 circuit (PCC), the secondary CO_2 circuit (SCC), the glycol heating circuit (GHC) and the auxiliary CO_2 circuit (ACC). During the charging mode, the PCC and the ACC are in operation. During the discharging mode, the SCC and the GHC are in operation.

Fig. 2 indicates the location of sensors for monitoring the mass flow rate, temperature, pressure and differential pressure in the test facility. The pressure of the PCC and SCC is measured by an absolute pressure transmitter (P1) calibrated in the pressure range 0–70 bar. Three differential pressure (DP) transmitters (calibrated in the range of 0.03–3 bar) are installed to measure the pressure loss across evaporator HEX (DP1), CTES unit (DP2) and condenser HEX (DP3). The refrigerant

temperature through both the charging and discharging processes in the primary and SCC is measured by five RTD Pt100 temperature sensors as follows: inlet and outlet of the CTES unit (T1 and T2), outlet of condenser HEX (T3), outlet of CO_2 pump (T4) and outlet of the evaporator (T5). The PCM temperature in the CTES unit is measured by T-type thermocouples (TC), located on the top surface of three selected PPs. Fig. 3 shows a top view of one PP indicating the position of each TC. The three PPs are selected according to their height in the plate stack, namely PP 2, PP 5 and PP 9. Each of these PPs is equipped with a set of nine consecutively numbered TC, which are distributed on the surface as follows: TC00–TC08 are mounted on PP 2, TC09–TC17 are mounted on PP 5 and TC18–TC26 are mounted on PP 9. The operator control of the test facility and the collection of the measurement data are achieved using a data acquisition system coupled with LabVIEW software [48]. An overview of the measurement equipment is given in Table 2.

The charging process is carried out through the PCC. The process consists of extracting heat from the PCM storage medium to the refrigerant. Consequently, the PCM solidifies (heat release) and the refrigerant evaporates (heat absorption). The circulation of the CO_2 is assured by a hermetic centrifugal refrigerant pump (CO_2 pump) with an inverter to control the refrigerant flow rate (Hermetic Pumpen GmbH [49]). From the outlet of the CO_2 pump, the refrigerant flow is split into two pipes: One pipe is used to recirculate the liquid refrigerant to the receiver of the CO2 refrigeration system and another one is used to feed the CTES. The recirculation pipe is required to assure the minimum flow requirement of the CO_2 pump. A Coriolis flowmeter (FT2) is used to measure the inlet CO_2 mass flow rate to the CTES unit. During the charging process, valves V1 and V3 are closed so that the PCC is active. The refrigerant enters the CTES at a liquid state through valve V2, then evaporates as it flows through the CTES unit as heat is transferred from the storage medium to the refrigerant. At the outlet of the CTES, the refrigerant is a mixture of liquid and vapour. The CO_2 mixture is then condensed to the liquid state in a plate HEX (condenser) connected to the auxiliary CO_2 cooling circuit. The liquid CO_2 is then brought from the outlet of the condenser to the
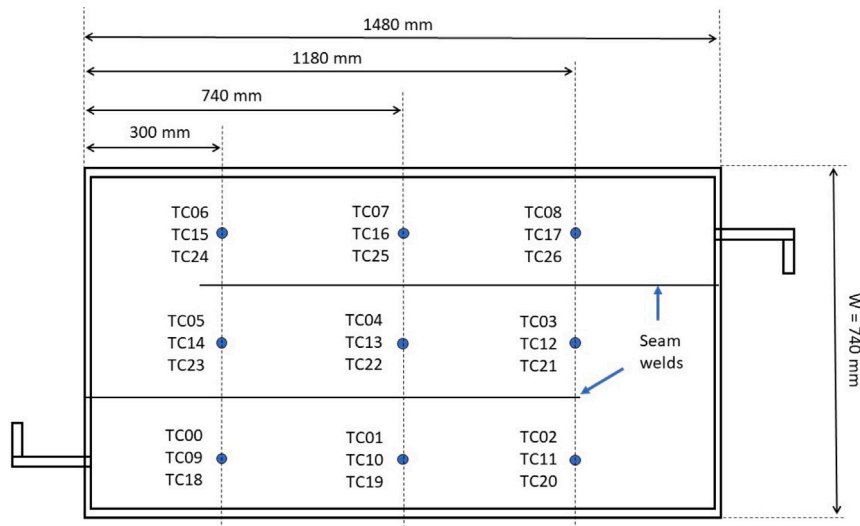
Fig. 3. Top view of a PP: Locations of thermocouples on three selected PPs. Figure first presented in [26].

refrigerant receiver. It is then drawn from the bottom of the receiver, and the cycle continues until the charging process is completed. The ACC provides the cooling of the PCC during the charging process. The cooling is achieved by supplying liquid refrigerant to the plate HEX (condenser) in the PCC through an electronic expansion valve (EEV 1). Furthermore, it maintains standby pressure in the PCC when the system is not in operation by supplying refrigerant to the subcooler through EEV 2. Both EEVs are operated by Danfoss superheat controllers. The auxiliary circuit is connected to the liquid and suction lines of a CO_2 booster refrigeration system in the laboratory to accomplish these two functions. The operator can select an evaporation level of −10 °C, −30 °C and −50 °C for the ACC by acting on a valve station (see Fig. 2). The evaporation pressure in the ACC can be modified by operating valve V5 located on the suction side of the ACC. This valve serves as a back-pressure valve, and reducing its opening degree will therefore increase the evaporation pressure in the ACC.

The discharging process is carried out through the SCC and consists of heat transfer from the refrigerant to the PCM. When the refrigerant flows inside the PPs, heat is rejected to the storage medium until the refrigerant is completely condensed at the manifold outlet. Consequently, the PCM absorbs the heat until it is completely melted. The SCC is connected to the GHC by the evaporator HEX, simulating the thermal load on the refrigeration system. During the discharging process, valve V2 and valve V4 are closed (see Fig. 2) so that the SCC is active. The flow direction through the CTES unit is reversed compared to the charging cycle so that the inlet and outlet are swapped. During the discharging cycle, the same DP transmitter used in the charging cycle measures the total pressure loss over the CTES unit. Two small manual ball valves are operated to exchange the high-pressure and low-pressure sides on the sensor. In the discharging process, liquid CO_2 is drawn from the bottom of the receiver by the CO_2 pump and circulated to the evaporator through valve V1. In the evaporator, heat is transferred from the glycol to the refrigerant so that the CO_2 exits the evaporator as a liquid/vapour mixture. The two-phase CO_2 is then circulated through the CTES unit, where heat is transferred to the storage medium and the refrigerant condenses to a fully liquid state. The cycle is then completed by returning the liquid refrigerant to the receiver through valve V3. The heat transfer fluid in the GHC is a mixture of 47% ethylene glycol (DowCal 100, DOW Chemicals) and water. The concentration of the ethylene glycol is measured with an ATAGO Master refractometer. The glycol is supplied to the evaporator by a Grundfos circulation pump. The glycol mass flow rate is measured by a Coriolis mass flow meter (FT 1). The heat input to the GHC is achieved by two 9 kW electric immersion heaters installed in the GHC,

Table 2
Measurement equipment utilised in the test facility.

Component	Model	Producer	Indicated accuracy
Absolute pressure transmitter	Cerabar S PMP71	Endress+Hauser	±0.25% of set span
Differential pressure transmitter	Deltabar S PMD75	Endress+Hauser	±0.15% of set span
Temperature sensor CO_2 and glycol	Class B RTD Pt100	RS PRO	±0.1 K
Temperature sensor PCM	Thermocouple type T	RS PRO	±0.2 K
Mass flow meter glycol	RHM 15 Coriolis meter	Rheonik	±0.2% of reading
Mass flow meter CO_2	RHM 06 Coriolis meter	Rheonik	±0.2% of reading

which gives the possibility to simulate a thermal load up to 18 kW. One of the heaters is fitted with pulse-width modulation (PWM) control for precise regulation of the power output from 0 to 100%. Furthermore, two RTD Pt100 temperature sensors are mounted in the inlet (T6) and outlet (T7) pipe of the HEX to measure the inlet and outlet temperature of the glycol, respectively.

3. Experimental procedure

3.1. Charging process

For the charging process, vertical plate pitches (δ_o) of 15 mm and 30 mm in the PP-HEX are considered. A series of experiments considering various refrigerant mass flow rates and evaporation temperatures were conducted for each plate pitch. The CO_2 evaporation temperature was varied from −12 °C to −23 °C, while the CO_2 mass flow rate was varied from 4 kg/min to 10 kg/min. The charging process in each test was run until completion to compare CO_2 pressure loss, PCM temperature and charging time for the different operating conditions and plate pitches. The charging cycle is initiated with the PCM in the CTES unit in the liquid phase. The start of the charging process takes place when the average PCM temperature (mean of TC00 to TC26) is measured below 0 °C. When the charging process is initiated, a layer of solid PCM is formed on the PP surface and it becomes thicker as the charging process progresses. This phenomenon continues until a complete block of solid PCM is formed between two adjacent PPs, i.e. when the solid PCM layer on the two PPs has overlapped (see

Fig. 10). At this point, the charging process continues as sensible energy storage until the temperature of the solid PCM block approaches the inlet refrigerant temperature. The charging process is completed when the difference between the mean PCM temperature and the refrigerant saturation temperature is less than 0.2 K. The charging time is defined as the period from the mean PCM temperature is measured below 0 °C and to the point where the temperature difference of the PCM and the refrigerant is less than 0.2 K. During the charging process, the formation of solid PCM can be easily visually observed through the plexiglass windows. The CTES is equipped with a camera that captures the formation of the solid PCM during the charging process at a fixed time interval. The mass flow rate of the CO_2 in the PCC is adjusted by controlling the frequency output of the inverter for the CO_2 pump (35–50 Hz). If the required mass flow rate is lower than the minimum frequency, the flow is throttled by partly closing valve V2 (see Fig. 2). The evaporation temperature of the CO_2 in the PCC (and thereby in the CTES unit) is set by adjusting the cooling rate of the ACC in the condenser HEX as explained in Section 2.2. The pressure in the PCC is maintained at a constant level when the same heat rate is extracted the CTES unit is rejected to the ACC in the condenser. When a higher cooling rate is provided by the ACC in the condenser than extracted from the PCM in the CTES unit, the pressure of the PCC will decrease.

3.2. Discharging process

For the discharging cycle, a plate pitch of 15 mm and 30 mm was applied. A series of experiments considering various CO_2 mass flow rates and condensing temperatures were conducted for each plate pitch. The CO_2 mass flow rate was varied from 4 kg/min to 10 kg/min and the CO_2 refrigerant condensing temperature was varied from –6.5 °C to 3.7 °C. The discharging process is initiated immediately when the charging cycle is completed, as described in Section 3.1. The refrigerant mass flow rate is controlled by frequency control of the CO_2 pump and throttling of the flow using valve V1, similar to the procedure applied in the charging process. The heat input to the CO_2 from the GHC controls the pressure in the SCC during the discharging cycle. If the heat transferred to the CO_2 in the evaporator equals the heat rejected to the storage medium in the CTES unit, the pressure in the SCC remains constant. Consequently, the pressure in the SCC can be set to the required value by supplying more or less heat to the SCC. Since one of the heaters is equipped with PWM control, the output of the electric heaters can be controlled with high precision by the operator. The discharging cycle is a highly transient process, and a PI controller is therefore implemented in the LabVIEW software to continuously adjust the heater output and keep a constant pressure in the SCC according to the specifications of the experiment. The discharging process continues until all the solid PCM blocks have completely melted or until the CO_2 is not able to reject any more heat to the CTES unit without increasing the pressure. The discharging time is defined as the time from the start of the discharging cycle until one of the two aforementioned criteria occurs. The discharging rate of the CTES unit is obtained by calculating the total heat transfer rate from the refrigerant to the PCM in the CTES unit. The heat is transferred from the GHS to the SCC in the evaporator, assuming no heat loss to the ambient occurs in the evaporator HEX. The CO_2 enters the evaporator at a saturated liquid state, delivered from the liquid receiver (see Section 2.2). Then the refrigerant enters the CTES unit as a two-phase mixture and exits the CTES unit in a subcooled condition. Consequently, it can be assumed that all the heat which is transferred from the glycol to the refrigerant in the evaporator HEX is rejected to the PCM in the CTES unit. The energy balance for the evaporator is given in Eq. (1). The thermodynamic properties of the ethylene glycol mixture were taken from the datasheet of the manufacturer [50], assuming a constant specific heat capacity of the fluid in the relevant temperature range.

$$\dot{E}_{CO_2,evap} = \dot{E}_g = \dot{m}_g \, cp_g \, (T_{g,outlet} - T_{g,inlet}) \tag{1}$$

where $E_{CO_2,evap}$ is the heat flow to the refrigerant in the evaporator, $\dot{E}_g$ is the heat flow of the glycol, $\dot{m}_g$ is the mass flow rate of the glycol, cp_g is the specific heat capacity of the glycol and $(T_{g,outlet} - T_{g,inlet})$ is the temperature difference from the inlet to the outlet of the glycol in the evaporator. Furthermore, the heat transfer required to cool the refrigerant from the condensation temperature (saturation temperature) to the outlet temperature (subcooled condition) is given in Eq. (2).

$$\dot{E}_{CO_2,subcool} = \dot{m}_{CO_2} \, cp_{CO_2} \, (T_{CO_2,sat} - T_{CO_2,outlet}) \tag{2}$$

where $E_{CO_2,subcool}$ is heat flow from the refrigerant to the PCM due to subcooling, $\dot{m}_{CO_2}$ is the mass flow rate of the refrigerant, cp_{CO_2} is the specific heat capacity of the refrigerant and $(T_{CO_2,sat} - T_{CO_2,outlet})$ is the difference between the saturation temperature and the outlet temperature of the refrigerant. The total discharge rate is then obtained by adding Eqs. (1) and (2) together, as presented in Eq. (3).

$$\dot{E}_{CO_2,tot} = \dot{E}_{CO_2,evap} + \dot{E}_{CO_2,subcool} \tag{3}$$

where $E_{CO_2,tot}$ is the total heat flow from the refrigerant to the PCM in the CTES unit. The total energy discharged over the cycle is obtained by numerical integration of the total discharge rate given in Eq. (3). All thermo-physical properties of the CO_2 are obtained using the thermodynamic database REFPROP 10 [51].

4. Uncertainty analysis and repeatability

The output of the temperature sensors was checked with an ice water bath and validated to operate at within ±0.2 K (thermocouples TC01–TC27, see Fig. 2) and ±0.1 K (RTD100 T1–T7, see Fig. 2) at 0 °C. The uncertainty analysis was carried out by the method elaborated in [52], using a confidence level of 95% (coverage factor of 2). The formulation used for the propagation of uncertainty is summarised below. Uncertainty for the mean PCM temperature on PP2, PP5, and PP9 ($T_{PP2,mean}$, $T_{PP5,mean}$, and $T_{PP9, mean}$):

$$u(T_{PCM}) = \sqrt{(1/9)^2 \cdot \sum_{i=1}^{9} u(T_i)} \,. \tag{4}$$

Uncertainty for the refrigerant saturation temperature:

$$u(T_{CO_2,sat}) = \sqrt{\left(\frac{\partial T_{CO_2,sat}}{\partial P_{CO_2,sat}}\right)^2 \cdot u(P_{CO_2,sat})^2} \,. \tag{5}$$

From the Antoine equation, the relationship between saturation temperature and saturation pressure can be found. By derivation and inserting the coefficients for CO_2, it can be written as:

$$\frac{\partial T_{CO_2,sat}}{\partial P_{CO_2,sat}} = \frac{2273.66}{P_{CO_2,sat} \cdot (17.9834 - \ln(P_{CO_2,sat}))^2} \,. \tag{6}$$

Uncertainty in the heat flow from the glycol to the refrigerant in the evaporator:

$$u(\dot{E}_{CO_2, evap}) = \sqrt{(cp_g \cdot \Delta T_g \cdot u(\dot{m}_g))^2 + (\dot{m}_g \cdot cp_g \cdot u(\Delta T_g))^2} \,. \tag{7}$$

Uncertainty in the glycol temperature difference from inlet to outlet in the evaporator:

$$u(\Delta T_g) = \sqrt{u(T_{g,in})^2 + u(T_{g,out})^2} \,. \tag{8}$$

Uncertainty in the heat flow from the refrigerant to the PCM due to subcooling of the refrigerant:

$$u(\dot{E}_{CO_2, subcool})$$
$$= \sqrt{(cp_{CO_2,liq} \cdot \Delta T_{CO_2} \cdot u(\dot{m}_{CO_2}))^2 + (\dot{m}_{CO_2} \cdot cp_{CO_2,liq} \cdot u(\Delta T_{CO_2}))^2} \,. \tag{9}$$

Uncertainty in the refrigerant temperature difference from the saturation temperature to the outlet temperature from the CTES:

$$u(\Delta T_{CO_2}) = \sqrt{u(T_{CO_2,sat})^2 + u(T_{CO_2, out})^2} \,. \tag{10}$$

Uncertainty in the total heat flow from the refrigerant to the PCM in the CTES unit:

$$u(\dot{E}_{CO_2,tot}) = \sqrt{u(\dot{E}_{CO_2,\ evap})^2 + u(\dot{E}_{CO_2,\ subcool})^2}. \quad (11)$$

The uncertainty in the discharged energy over the cycle is estimated by integrating the uncertainty in the heat flow from the refrigerant to the PCM (Eq. (3)) from the start to the end of the cycle. To investigate the repeatability of the experiments, tests with identical test conditions were carried out for both plate configurations. The charging time was used as the indicator for the charging cycle. The resulting range of charging time was found to be <5 min for the 15 mm plate pitch <10 min for the 30 mm configuration. This corresponds to a repeatability of the charging time within ±6.7% and ±5.1% at T_{sat} = −15.5 °C and $\dot{m}_{CO_2}$ = 8 kg/min for the 15 mm and 30 mm plate pitch, respectively. For the discharging process, the mean discharge rate and discharged energy over the cycle were chosen as indicators for repeatability. The obtained range for the discharged energy over the cycle was <0.3 kWh for both configurations, corresponding to <4% and <3% of the discharged energy at the tested conditions for the 15 mm and 30 mm plate pitch, respectively. For the mean discharge rate, the obtained range was <0.25 kW for both configurations.

5. Characterisation of the PCM

In this study, the selected PCM consists of the commercial paraffin PCM RT-9HC (Rubitherm Technologies GmbH [53]) which has a phase change temperature in the range of −9 °C and −10 °C [53]. The selection of RT-9HC as the PCM was based on the temperature requirement for a CTES system designed to be integrated into CO_2 refrigeration systems in the food processing industry (typically −15 °C to 0 °C). The PCM was selected among other potential candidates as it has the highest latent heat capacity. Moreover, RT-9HC was selected thanks to its compatibility with the materials used in the CTES unit in this study. A thorough experimental characterisation of the PCM is required in order to fully explore and understand the behaviour of the heat transfer process from the PCM to the refrigerant and vice versa. Several experimental characterisation techniques are applied to determine the latent heat capacity, phase transition temperature, thermal conductivity, density and viscosity of the PCM. The applied methods and the results for each property are described in detail in the following paragraphs.

The Differential Scanning Calorimetry (DSC) technique is used to determine the latent heat capacity and the phase transition temperature of the PCM. DSC is found to be the appropriate technique to identify the storage capacity characteristics and phase change range for organic PCM according to the German quality label PCM-RAL (RAL-GZ 896 [54]). Several authors emphasise the importance of low heating/cooling rates (typically 1 K/min or lower) to obtain reliable and accurate results when using DSC for PCM characterisation [55–58]. Feng et al. [57] showed that the sample mass has less influence on the measured latent heat capacity and melting temperature than the heating rate. The apparatus used in the current study is a TA Instruments Q2000 DSC equipped with liquid nitrogen cooling, and the standard 40 µL aluminium crucibles were used to host the material samples. The DSC is calibrated and checked with indium. The obtained results of the melting temperature and melting enthalpy of indium were within 0.5% of the reference values provided by the manufacturer [59,60]. Furthermore, a 10 mg sample of deionised water was tested and found to give melting enthalpy with less than 0.2% deviation of tabulated values (333.55 kJ/kg). Two samples of RT-9HC were prepared and weighed using a Mettler Toledo laboratory scale with a precision of ±0.01 mg. The samples were then cycled from 30 °C to −40 °C using a constant heating/cooling rate ranging from 10 to 1 K/min, often referred to as the dynamic method. For more in-depth information and description of DSC methods applicable to PCM characterisation, the reader is directed to Barreneche et al. [55].

The samples were subject to temperature equilibration and a 5-minute isothermal stage before and after each heating/cooling segment. The results are presented in Table 3. It can be seen that the onset melting temperature is slightly shifted to a higher temperature by reducing the heating rate, namely from −9.80 °C to −9.58 °C in the case of the smallest sample mass. Furthermore, the peak melting temperature is shifted towards a lower temperature with lower heating rates. This effect is more pronounced for higher sample mass due to the higher thermal inertia of the larger sample when applying a high heating rate to the sample. The latent heat capacity is not significantly influenced by neither the heating rate change nor the sample weight. A mean value of 202.6 kJ/kg was obtained considering all the DSC tests. For the solidification process, a supercooling phenomenon was observed. This is an unwanted behaviour as the temperature of the PCM needs to be decreased below the freezing point to start the crystallisation process [61]. However, it is expected that the supercooling effect will not be as pronounced when the PCM is cycled at full scale in the CTES unit. The crystallisation onset ranged from −12.32 °C to −12.83 °C for the largest sample and between −13.22 °C and −13.51 °C for the smallest sample. The supercooling effect was greater when applying the highest cooling rate.

The heat transfer process within the PCM in the CTES unit is expected to be dominated by conduction heat transfer because the PCM is not subject to mechanical stirring or any other form of forced circulation. Therefore, the thermal conductivity of the PCM will have a significant impact on the heat transfer rate for both the charging and the discharging processes. The thermal conductivity of the PCM used in this study is measured by a thermal constants analyser (TPS 2500s, Hotdisk AB) which is based on the transient plane source technique [62]. It was identified for both liquid and solid phases of the PCM. A liquid sample holder specially designed by the manufacturer of the thermal constants analyser (Hotdisk AB) was utilised to perform the measurements on the liquid PCM and ensure adequate test conditions of the sample. The liquid test cell consists of a block of aluminium with a small sample volume inside where the sensor is vertically inserted. The manufacturer recommends using a small sensor, applying low sensor heating power and limiting the measurement time to a few seconds to ensure the reliability and repeatability of the tests. These recommendations are given to avoid initiating natural convection in the sample that affects the measurements when measuring the thermal conductivity of low-viscosity liquids. A sensor with a radius of 2.0 mm (Kapton sensor 7577, Hotdisk AB), a sensor heating power of 25 mW and a measurement time of 2 s were then applied to perform the measurements. The liquid test cell was put into a metal sample holder and placed into a thermal bath. A Pt100 temperature sensor was used to measure the sample temperature during the temperature stabilisation period. The temperature of the thermal bath was varied from 25 °C to −9 °C, and a 6-hour stabilisation period was introduced at each temperature stage before the measurements were taken to ensure a thermal equilibrium within the sample. The measurements were performed four times at each temperature step with a 20 min holding time between each measurement. The mean value and standard deviation were calculated. For the measurements in the solid phase, a sensor with a radius of 6.4 mm (Kapton sensor 5501, Hotdisk), a sensor heating power of 25 mW and a measurement time of 80 s were selected to perform the measurements. The Kapton sensor was centred in a cylindrical sample holder that was filled with solid PCM. The solidified sample was then placed into the thermal bath to achieve thermal equilibrium. A test series using distilled water in the liquid sample holder was first carried out in the temperature range 5 °C to 30 °C for verification of the instrument. The thermal conductivity obtained for distilled water was then compared to the correlation proposed by Dixon [63]. The results were found to be within 3% and 6.5% of the correlation for a sample temperature below and above 20 °C, respectively. It is suspected that there is some onset of convection within the sample for temperatures above 20 °C due to decreased viscosity of the water, resulting in an

Table 3

Results of DSC thermal analysis of PCM RT-9HC.

Sample mass [mg]	Heating rate [°C/min]	$T_{onset,melt}$ [°C]	$T_{peak,melt}$ [°C]	Melting enthalpy [kJ/kg]
7.941	10	−9.80	−8.11	203.8
7.941	5	−9.71	−8.50	204.2
7.941	2.5	−9.63	−8.74	204.0
7.941	1	−9.58	−8.82	202.0
13.351	10	−9.87	−7.99	201.9
13.351	5	−9.77	−8.43	202.2
13.351	2.5	−9.68	−8.52	201.6
13.351	1	−9.59	−8.37	201.1
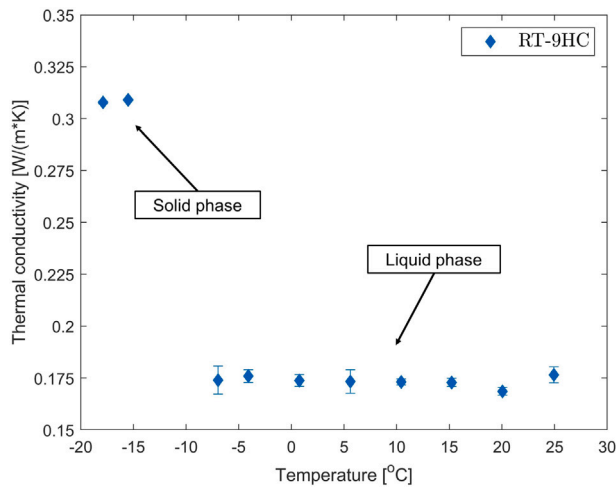
Fig. 4. Thermal conductivity of PCM RT-9HC in the liquid and solid phases as a function of temperature.

Fig. 5. Liquid density of RT-9HC depending on the temperature. Standard deviation of the measurements are indicated as error bars.

overestimation of the thermal conductivity. The results were within the acceptable limit of 5% for sample temperatures below 20 °C, which is the typically expected accuracy of the apparatus. The results of the thermal conductivity measurements for RT-9HC is presented in Fig. 4. It can be observed that in the applied temperature range −7 °C to 25 °C thermal conductivity in the liquid phase was approximately constant (≈ 0.174 W/(m K)). Furthermore, it can be observed that the thermal conductivity of the PCM in the solid phase is about 75% higher compared to that in the liquid phase (0.309 W/(m K) at −15.5 °C). It is expected that the thermal conductivity of the solid phase is higher than the liquid phase, as the lattice structure in solids fixes the position of the molecules, which increases the thermal conductivity of the material. It was also found that the thermal conductivity of the water is ≈ 235% higher than for the PCM at 5 °C, confirming that low thermal conductivity is one of the main limitations of using organic PCMs as the storage material [7].

Natural convection within the liquid PCM can be a significant contribution to the overall heat transfer in a PCM-HEX. The significance of natural convection in the liquid PCM is mainly dependent on three factors: the temperature variation within the PCM to drive the natural convection process, the change of density with change in temperature and the viscosity of the PCM. The density change of the liquid PCM was calculated by measuring the volumetric expansion of the liquid PCM in a 25 ml measuring cylinder placed in a thermal bath. The temperature was varied from 30 to −9 °C, with 5 K intervals and a holding time of 30 min per step. The procedure was repeated for three samples with a mass of 14.82 g, 16.38 g and 17.90 g, respectively. The sample mass was measured with a laboratory scale with a precision of 0.01 g (ME4002, Mettler Toledo). The mean value of the liquid density depending on temperature is presented in Fig. 5. It can be observed that the liquid density shows a nearly linear increase with temperature in the investigated range. The density of the solid phase
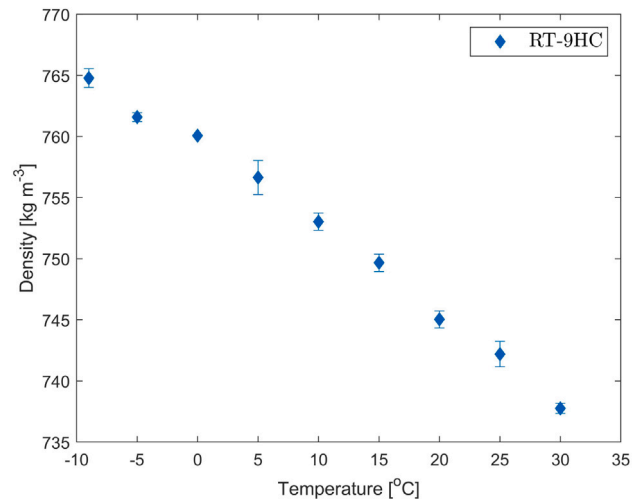
was determined by placing a liquid sample (39.8 g), which was kept in a 100 ml measuring cylinder, into a thermal bath at −15 °C to solidify. The volume of the solid sample was registered, and the density was calculated to 880 kg m^{-3}. Due to the precision of reading the PCM volume in the measuring cylinders, an uncertainty of ±10% is assumed for the density results.

The viscosity of the PCM in the liquid phase is determined using a rotational rheometer (Haake Mars III, Thermo Fischer Scientific) having a concentric cylinder geometry (DIN Z40, 8 mm gap). The rheometer geometry is connected to a thermal bath to control the temperature of the sample. The apparent viscosity of the PCM was determined by varying the shear rate from $\gamma = 10$ 1/s to $\gamma = 100$ 1/s within the temperature application range. Each test series was repeated three times, and the results with the standard deviation are presented in Fig. 6. It can be seen that the apparent viscosity of the PCM is nearly constant for the investigated range of shear rate, demonstrating a near-Newtonian behaviour of the PCM for the considered range of shear rate. Moreover, it was observed that the apparent viscosity of the PCM increases as the temperature is reduced. The mean value of the viscosity is $\eta_{PCM} = 5.57$ mPa s, $\eta_{PCM} = 2.53$ mPa s and $\eta_{PCM} = 1.98$ mPa s for a temperature of −8.05 °C, −0.06 °C and 7.78 °C, respectively. At a temperature of ≈ 0 °C, the viscosity of the PCM was found to be 41.3% higher compared to that of liquid water ($\eta_{H_2O} = 1.79$ mPa s at $T = 0.01$ °C [64]). A summary of the PCM characterisation with complementary data from the datasheet of the manufacturer is presented in Table 4.

6. Results and discussion

6.1. Charging cycle

This section presents the results obtained from the charging tests described in Section 3.1. The purpose of the first test series is to

Table 4

Summary of PCM characterisation and comparison with data from manufacturer [53].

| Property	Measured	Datasheet	Comments; Rubitherm (R) and measurements (M)
Melting temperature	−9.6 °C	between −9 °C and −10 °C	R: using a 3-layer-calorimeter
Latent heat capacity	202.6 kJ/kg	250 kJ/kg	R: ±7.5%, including sensible heat −16 °C to −1 °C
Thermal conductivity liquid	0.174 W/(m K)	0.2 W/(m K)	R: Same value for both phases
Thermal conductivity solid	0.309 W/(m K)	0.2 W/(m K)	R: Same value for both phases
Density liquid	745 kg/m³	770 kg/m³	M: ±10%. Both values at 20 °C
Density solid	880 kg/m³	880 kg/m³	M ±10%. Both values at 20 °C
Flash point	–	70 °C	–
Maximum operating temperature	–	30 °C	–
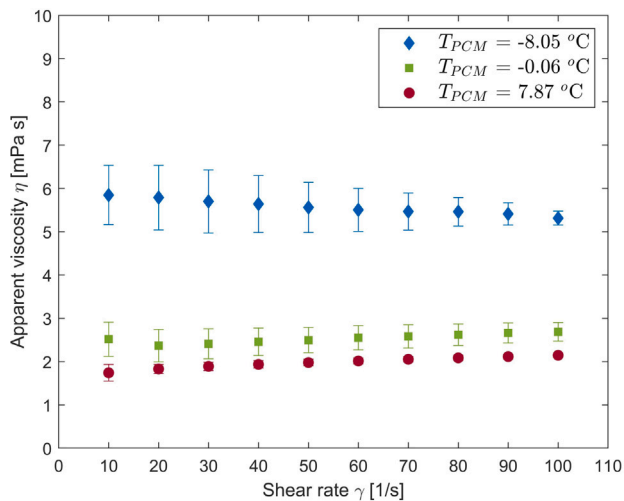
Fig. 6. Apparent viscosity of the PCM RT-9HC depending on the temperature. The standard deviation of each measurement point is indicated.

Fig. 7. The effect of refrigerant mass flow rate on charging time and pressure loss through the CTES unit using a CO_2 evaporation temperature of −16 °C and a plate pitch of 15 mm.

determine the appropriate refrigerant flow rate supplied to the CTES unit to operate the charging cycle effectively. The selected HEX design is relative to a plate pitch of 15 mm. The refrigerant evaporation temperature was kept constant at −16 °C for all tests, while the total mass flow rate was varied from 4 kg/min to ≈ 9.5 kg/min. The refrigerant pressure loss through the CTES is measured using the differential pressure sensor (DP2) shown previously in Fig. 2. Both the charging time and the mean pressure loss over the CTES unit are represented in Fig. 7 for a set of applied CO_2 mass flow rates. It can be observed that the charging time decreases when the refrigerant mass flow rate is increased. Increasing the flow rate from $\dot{m}_{CO_2} = 5$ kg to $\dot{m}_{CO_2} = 8$ kg/min has decreased the charging time by 33%. A further increase of the flow rate further from $\dot{m}_{CO_2} = 8$ kg/min to $\dot{m}_{CO_2} = 9.5$ kg/min was observed to have no significant enhancement on the charging time which has decreased only by 5%. The increase in the charging time for the lowest mass flow rate can be explained by inadequate refrigerant supply to operate the charging cycle. In fact, for $\dot{m}_{CO_2} = 4$ kg/min and $\dot{m}_{CO_2} = 5$ kg/min, superheated refrigerant was measured at the outlet of the CTES unit during the first 10–15 min of the charging process. This observation means that all the refrigerant supplied to the CTES unit during this period had been fully evaporated inside the PPs before reaching the manifold at the outlet.

Operating the charging cycle under superheated conditions is found to decrease the efficiency of the charging cycle as the heat transfer from the PCM to the refrigerant is ensured by sensible heat (elevation of the refrigerant vapour temperature), and no more by the evaporation of the liquid refrigerant. Applying vapour/liquid refrigerant mixture conditions along the full length of the HEX (often referred to as flooded conditions) is a key factor for the proper use of the available heat transfer area and thus increase the heat transfer process [65–68]. It
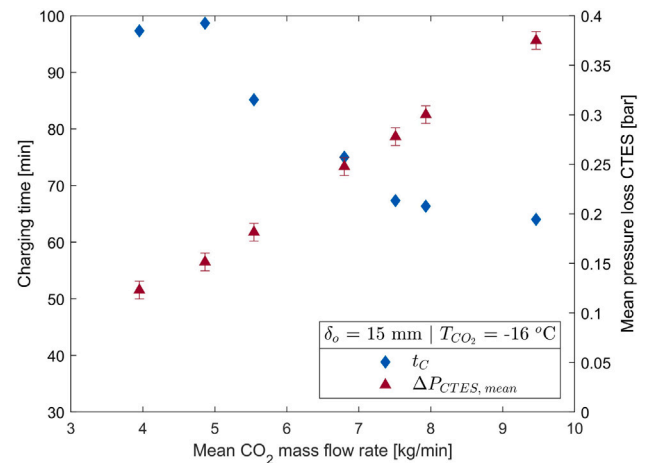
was also observed that for the experiments using a CO_2 flow rate less than 7.5–8 kg/min the thickness of the solid PCM layer on the PP surface was less uniform, particularly close to the outer edges and corners of the PPs (dead zones) where the refrigerant shifts direction (see Fig. 1a). Consequently, a higher refrigerant flow rate improves the refrigerant distribution in the PP channels. Moreover, these observations indicate that the turbulence occurring in the dead zones by the higher refrigerant flow rates also promotes the heat exchange between the PCM and the refrigerant in these areas, leading to a shorter and more efficient charging process. It can also be depicted from Fig. 7 that the mean refrigerant pressure loss through the PPs increases when increasing the refrigerant mass flow rate. Indeed, a higher mass flow rate increases the mean velocity of the refrigerant inside the PP channel, which in turn increases the pressure loss. The pressure loss increases nearly linearly from 0.123 bar for $\dot{m}_{CO_2} = 4$ kg/min to 0.3749 bar for $\dot{m}_{CO_2} = 9.5$ kg/min. The pressure loss is an unwanted phenomenon since it increases the required pressure lift of the compressors in the refrigeration system, consequently increasing the energy consumption. However, for the investigated range of flow rates, the pressure loss is less than the typical maximum allowable pressure drop in PP-HEX (0.4–0.6 bar [69]). By increasing the mass flow rate from 8 kg/min to 9.5 kg/min, the pressure loss increases by 25 %, while the corresponding reduction in charging time is less than 4%. This indicates that the heat transfer process is limited from the PCM side. Based on the analysis above, a mass flow rate of 8 kg/min resulting in a lower charging time, a pressure loss lower than 0.4 bar and promoting a satisfying heat transfer in the CTES dead zones was selected for further investigations on the charging cycle.

A series of tests were performed using a CO_2 mass flow rate of 8 kg/min and a CO_2 evaporation temperature ranging from −12 °C to −23 °C for both plate pitches of 15 mm and 30 mm. The tests

were carried out to investigate the effect of the refrigerant evaporation temperature on the charging cycle performance. The charging time and mean pressure loss as a function of the refrigerant evaporation temperature are presented in Fig. 8a and b, respectively. It can be clearly seen from Fig. 8a that the same refrigerant evaporation temperature and comparing the 15 mm and 30 mm plate pitch designs, the charging time for $\delta_o = 15$ mm results in a faster charging process than that of $\delta_o = 30$ mm as the theoretical latent storage capacity of the CTES unit is doubled for the 30 mm configuration. For an evaporation temperature ($T_{CO_2,evap}$) of −13 °C, the charging time has increased by $\approx 150\%$ for the 30 mm configuration compared to the 15 mm configuration. For a $T_{CO_2,evap} = −20$ °C the recorded increase in the charging time for $\delta_o = 30$ mm was $\approx 161\%$.

The results also show that the charging time is reduced when operating the charging cycle with lower refrigerant evaporation temperatures. Decreasing the evaporation temperature from −13 °C to −15.5 °C yields a reduction in the charging time by 40.7 % for the 15 mm configuration and by 44.0% for the 30 mm configuration. A further reduction in the evaporation temperature from −15.5 °C to −17.5 °C reduces the charging time by 21.0% and 23.7% for the 15 mm and 30 mm plate pitch, respectively. As heat is removed from the PCM during the charging cycle, a layer of solid PCM is formed on both sides of each PP. For two successive PPs, the liquid PCM volume comprised between the formed solid PCM blocks is reduced, and the thickness of the solid PCM layer increases. As the solid PCM layer grows, the charging process decelerates as the solid PCM layer acts as additional thermal resistance to the heat transfer process. This effect is even more pronounced for the 30 mm configuration compared to the 15 mm configuration due to the thicker solid PCM layer required to complete the charging process. The temperature difference between the solidifying PCM and the refrigerant can be increased by reducing the refrigerant evaporation temperature to increase the driving forces for the heat transfer process. Although significant reductions in the charging time can be achieved by reducing the evaporation temperature, the energy consumption of the compressors in the refrigeration system will also increase due to the increased pressure lift of the system. Previous studies have shown that lowering the evaporation temperature of 1 °C will reduce the coefficient of performance (COP) of the system by about 2%–3% [65]. Based on the discussion above, a significant reduction in the charging time is achieved using a temperature difference between the phase change temperature of the PCM and the refrigerant of 5–6 K for both plate pitches. Nevertheless, a parametric study to identify the appropriate refrigerant evaporation temperature and plate pitch should be carried out for each CTES installation using the present HEX design, considering the required storage capacity and cost of electricity as the design parameters.

Fig. 8b presents the mean refrigerant pressure loss across the CTES unit during the charging cycle for both 15 mm and 30 mm plate pitch for different refrigerant evaporation temperatures. It can be seen that the mean pressure loss tends to increase for a fixed refrigerant flow rate as the evaporation temperature decreases. In fact, a reduction in the evaporation temperature strengthens the driving forces for the heat transfer process, and thus more refrigerant is evaporated in the PP channels. Consequently, the mean density of the vapour/liquid refrigerant mixture decreases and the mean velocity of the refrigerant increases, generating a higher pressure loss. A nearly linear increase in the pressure loss is recorded in the studied refrigerant temperature range. The pressure loss increased by 156% (from 0.214 bar to 0.548 bar) for $\delta_o = 15$ mm and by 103% (from 0.211 bar to 0.428 bar) for $\delta_o = 30$ mm when decreasing the refrigerant temperature from −12 °C to −22.5 °C. The recorded mean pressure loss for the 15 mm configuration was higher than for the 30 mm configuration as the charging cycle for the former design is shorter than that for the latter. For $\delta_o = 30$ mm, the heat transfer is decelerated due to the solid PCM layer formation on the PP as the charging process progresses, as explained earlier in this section. Consequently, less refrigerant is
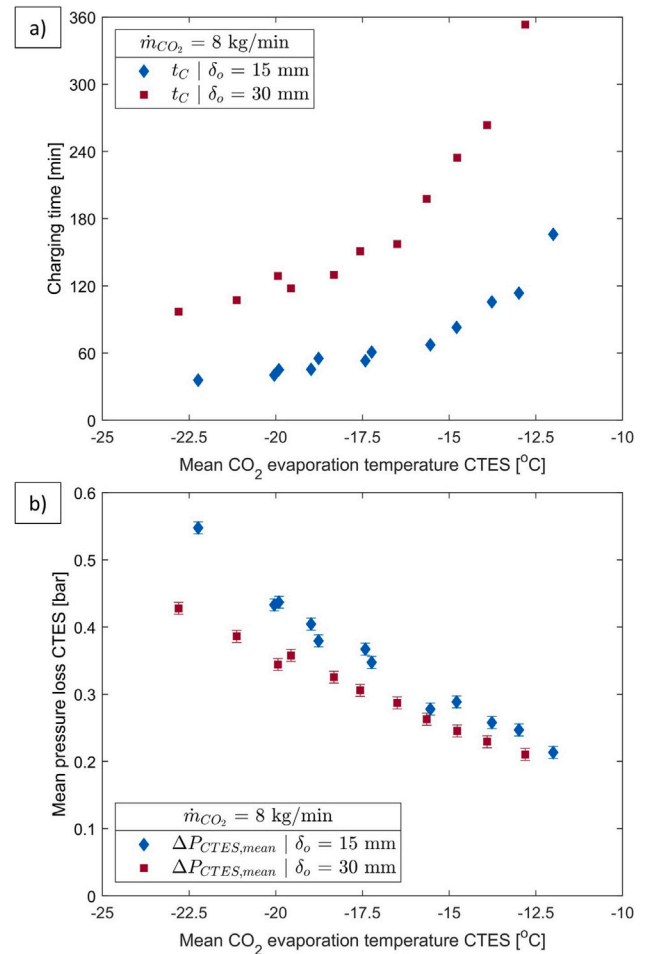

Fig. 8. The effect of refrigerant evaporation temperature for the 15 mm and 30 mm configuration using a refrigerant mass flow rate of 8 kg/min on (a) the charging time (b) mean pressure loss.

evaporated in the PP channels, and the mean density of the refrigerant increases gradually during the charging cycle. The refrigerant velocity is then reduced and decreases the mean refrigerant pressure loss over the cycle.

During the charging process, both the bulk PCM temperature (mean of TC00–TC26, see Fig. 3) near to PP2, PP5 and PP9 as well as their relative refrigerant temperature evolution are recorded for three selected experiments ($T_{CO_2,evap} = −13$ °C, $T_{CO_2,evap} = −16$ °C and $T_{CO_2,evap} = −22$ °C). They are represented for $\delta_o = 30$ mm plate pitch as shown in Fig. 9. For all experiments, the initial temperature of the storage medium was set to ≈ 4 °C and a refrigerant mass flow rate of 8 kg/min. The phase change temperature (onset melting temperature) of the PCM RT-9HC was determined by DSC measurements to $T_{pc,PCM} = −9.58$ C. At first glance, it can be observed that the duration of the charging cycle significantly decreases when decreasing the refrigerant evaporation temperature. The charging time of the CTES unit is reduced from 354 min to 110 min when the CO_2 evaporation temperature is reduced from −13 °C to −22 °C. For the three experiments, a rapid decrease in the PCM bulk temperature was observed in the first 15–20 min of the charging cycle, denoting an SHS process. After this initial period, the charging process continues as an LHS process with a constant temperature difference between the evaporating CO_2 inside the PP channels and the phase change temperature of the PCM that solidifies at the solid–liquid interface. During this period, a "plateau" can be observed in the PCM bulk temperature profile describing a latent heat storage, most notable for the highest CO_2 evaporation temperatures ($T_{CO_2,evap} =$

Table 5
The calculated maximum theoretical latent storage capacity of the CTES unit in various configurations.

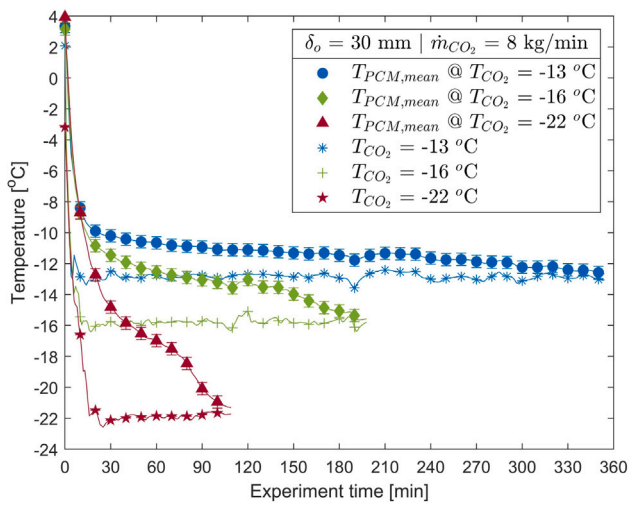| δ_o [mm]	$\delta_{o,mean}$ [mm]	m_{PCM} [kg]	$E_{lat,th}$ [kWh]	t_C @ $T_{CO_2,evap}$ = −15.5 °C [min]
15	12.85	111.88	6.31	67
30	27.85	225.07	12.69	198

Fig. 9. Bulk PCM temperature and refrigerant evaporation temperature evolution during the charging cycle for three different refrigerant evaporation temperatures ($T_{CO_2,evap}$ = −13 °C, $T_{CO_2,evap}$ = −16 °C and $T_{CO_2,evap}$ = −22 °C) using a refrigerant mass flow rate of 8 kg/min and δ_o = 30 mm.

−13 °C and $T_{CO_2,evap}$ = −16 °C). The measured bulk PCM temperature is approaching the refrigerant evaporation temperature during the LHS period because the thermocouple sensors become embedded in the solid PCM layer as the charging progresses. There is a temperature gradient within the solid PCM layer in the perpendicular direction of the PP surface, where the temperature ranges from the refrigerant evaporation temperature at the PP surface to the PCM phase change temperature at the liquid–solid interface. The LHS period continues until the solid PCM layer formed on the PP surface overlaps with the solid PCM layer on the neighbouring PP (see Fig. 10), forming a solid block of PCM between the PPs. The PCM temperature decreases more rapidly and approaches the refrigerant temperature, and energy is then stored by an SHS process. From Fig. 9, this condition occurs at ≈ 293 min for $T_{CO_2,evap}$ = −13 °C, at ≈ 145 min for $T_{CO_2,evap}$ = −16 °C and at ≈ 77 min for $T_{CO_2,evap}$ = −22 °C. The development of the charging process and growth of the solid PCM layer on the PP surface after 30, 50 and 90 min for three CO_2 evaporation temperatures (−13 °C, −17 °C and −21 °C) are shown in Fig. 10. The pictures clearly show that operating the charging process with lower refrigerant evaporation temperature results in faster growth of the solid PCM layer. It can be observed that after 90 min, the charging cycle using an evaporation temperature of −21 °C is nearly finished, i.e. the PCM layers from neighbouring PPs have nearly grown together.

Table 5 presents the calculated useful mass of PCM in the CTES unit, i.e. the PCM that occupies the volume between the PPs that is cycled through its phase change process. Furthermore, the theoretical latent storage capacity of the CTES unit and the resulting charging time using an evaporation temperature of −15.5 °C for the 15 mm and 30 mm plate pitches are presented. It can be seen that the theoretical storage capacity is doubled when the plate pitch is increased from 15 mm to 30 mm. However, the charging time increases by 194% from 67 min to 198 min for the same evaporation temperature ($T_{CO_2,evap}$ = −15.5).

6.2. Discharging cycle

This section presents the results obtained for the discharging tests following the procedure described in Section 3.2. The first test series

are performed to identify the appropriate refrigerant flow rate for the discharging cycle. During these experiments, the CO_2 condensation temperature ($T_{CO_2,cond}$) was kept at −1 °C and the mass flow rate was varied from 4 kg/min to 10 kg/min for a plate pitch δ_o = 30 mm. The discharging rate profiles for the tests using a refrigerant mass flow rate of 4, 7 and 10 kg/min are presented in Fig. 11. It is observed that the discharging cycle follows the same general trend for all of the considered flow rates. A high discharging rate (24–16 kW) is recorded during the first 10–15 min. A gradual decrease in the discharging rate is then observed towards zero to denote the end of the discharging cycle. At the beginning of this process, the adjacent solid PCM to the PP surface starts to melt. As the condensation heat from the CO_2 is transferred to the PCM, a thin layer of liquid PCM is formed between the PP surface and the solid PCM block. As the discharging process progresses, the liquid PCM layer becomes thicker, and thus, the thermal resistance to the heat transfer process is also increased. This process is analogous to the growth of the solid PCM layer during the charging process, which is also limiting the heat transfer between the PCM and the refrigerant. As the liquid PCM layer increases in thickness, the discharging rate decreases gradually towards ≈ zero, denoting the end of the discharging cycle. It can also be seen from Fig. 11 that a mass flow rate of 7 kg/min yields the highest overall discharge rate during the first 60 min of the discharging cycle, approximately 2–3 kW higher than for the flow rate of 4 kg/min.

The mean discharging rate and discharged energy over the cycle for the considered range of refrigerant mass flow rates (4 kg/min to 10 kg/min) for $T_{CO_2,cond}$ = −1 °C and δ_o = 30 mm are presented in Fig. 12. The figure shows that the mean discharging rate is continually increasing in a nearly linear behaviour from 5.09 kW to 7.76 kW when the mass flow rate increases from 4 kg/min to 10 kg/min, respectively. The total discharged energy (E_D) over the cycle is increasing from 12.19 kWh at a flow rate of 4 kg/min to the maximum value of 13.86 kWh at 7 kg/min. For a mass flow rate of $\dot{m}_{CO_2}$ = 10 kg/min, E_D decreases to 11.87 kWh. Although the highest refrigerant mass flow rate resulted in the highest mean discharge rate, it yielded the lowest amount of discharged energy over the cycle. This is because using lower mass flow rates (<8 kg/min) it was possible to sustain the discharging cycle for a longer time, see Fig. 11. Using a flow rate of 4 and 7 kg/min resulted in a longer discharging time (40–50 min) than using the flow rate of 10 kg/min, and the discharge rate is less than 2.5 kW during this period. Consequently, the mean discharge rate over the cycle will be lower for the tests with a longer discharging time. Based on the discussions above, the mass flow rate that yielded the highest amount of discharged energy over the cycle (7 kg/min) was selected for further investigations.

The effects of the CO_2 condensation temperature variation ($T_{CO_2,cond}$ = −4.59 °C, $T_{CO_2,cond}$ = −0.88 °C and $T_{CO_2,cond}$ = 2.46 °C) on the evolution in the discharging rate have also been studied and presented in Fig. 13. The selected refrigerant mass flow rate was $\dot{m}_{CO_2}$ = 7 kg/min as it has provided the highest discharged energy (see the previous paragraph). It was observed that the discharging rate is higher as the $T_{CO_2,cond}$ is increased. During the discharging process, the mean discharging rate for $T_{CO_2,cond}$ = −4.59 °C, $T_{CO_2,cond}$ = −0.88 °C and $T_{CO_2,cond}$ = 2.46 °C are 3.67 kW, 6.22 kW and 9.01 kW, respectively. Furthermore, operating the discharging cycle with higher $T_{CO_2,cond}$ results in a decrease in the discharging time because of the higher discharge rate. As the PCM melting temperature is fixed at −9.6 °C, increasing the $T_{CO_2,cond}$ increases the driving forces for the heat transfer process from the refrigerant to the PCM. Also, increasing the temperature difference between the storage medium and the refrigerant
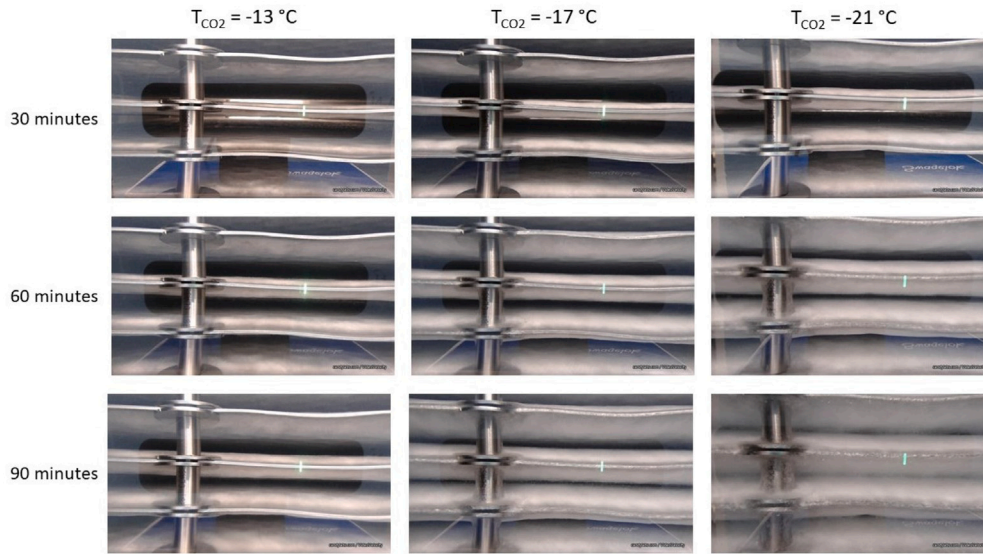
Fig. 10. Development of the solid PCM layer on the PP surface after 30, 60 and 90 min when using a CO_2 evaporation temperature of -13 °C, -17 °C and -21 °C and using a refrigerant mass flow rate of 8 kg/min and a plate pitch of 30 mm.
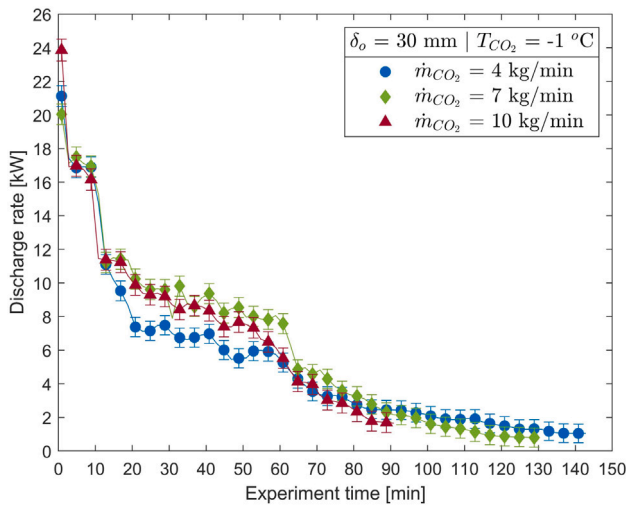

Fig. 11. Discharging rates for three refrigerant mass flow rates (4, 7 and 10 kg/min) for a refrigerant condensation temperature $T_{CO_2,cond} = -1$ °C and a plate pitch $\delta_o = 30$ mm.
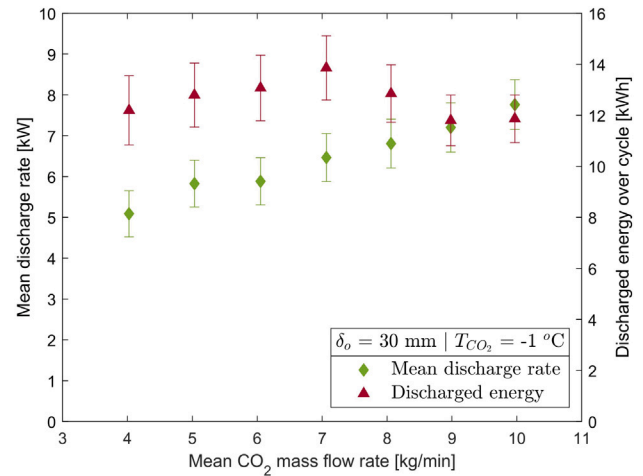

Fig. 12. Mean discharging rate and discharged energy variation with the refrigerant mass flow rate for a refrigerant condensation temperature $T_{CO_2,cond} = -1$ °C and a plate pitch $\delta_o = 30$ mm.

compensates to some extent the thermal resistance that occurs when the liquid PCM layer is formed between the solid PCM block and the PP surface, and thus ensures a higher discharge rate throughout the cycle. Consequently, a clear "plateau" in the discharging rate curve is observed for the first 45 min using $T_{CO_2,cond} = 2.46$ °C. This effect is also observed for $T_{CO_2,cond} = -0.88$ °C for the first 65 min, but is less pronounced compared to $T_{CO_2,cond} = 2.46$ °C. For $T_{CO_2,cond} = -4.59$ °C, the discharging rate is slowly decreasing from about 6.4 kW at 12 min to zero at 162 min, denoting the end of the cycle. For the first 60 min of the discharging cycle, the mean discharging rate for $T_{CO_2,cond} = -4.59$ °C, $T_{CO_2,cond} = -0.88$ °C and $T_{CO_2,cond} = 2.46$ °C are 5.94 kW, 10.58 kW and 13.80 kW, respectively.

The mean discharging rate and discharged energy over the cycle as a function of the CO_2 condensation temperature in the range of -6.49 °C to 3.67 °C are presented in Fig. 14. It can be observed that the mean discharging rate over the cycle increases in a nearly linear trend from 2.50 kW to 9.79 kW as the $T_{CO_2,cond}$ increases from -6.49 °C to 3.67 °C. Increasing the difference between the $T_{PCM,pc}$ and

$T_{CO_2,cond}$ by 327% has enhanced the driving forces for the heat transfer process from the refrigerant to the PCM and generated an increase of 292% in the discharging rate. It can also be seen from Fig. 14 that the discharged energy over the cycle increases with higher CO_2 condensation temperature. A higher $T_{CO_2,cond}$ (and thereby high driving forces for the heat transfer) ensures that all solid PCM is melted during the discharging cycle. It was also visually observed that for the lowest CO_2 condensation temperature ($T_{CO_2,cond} = -6.49$ °C), a significant share of the solid PCM did not melt even when the discharging cycle ended. This phenomenon is an unwanted behaviour of the storage medium as it clearly limits the discharging capacity of the storage. The smallest solid PCM fraction left by the end of the discharging cycle was observed around the edges of the PP for the highest refrigerant condensation temperature. The complete melt of the PCM block at the end of the discharging cycle was depicted for $T_{CO_2,cond}$ higher than -2.58 °C. The discharged energy over the cycle was $E_D = 10.05$ kWh, $E_D = 13.92$ kWh and $E_D = 17.03$ kWh when using a CO_2 condensation temperature of $T_{CO_2,cond} = -4.59$ °C, $T_{CO_2,cond} = -0.83$ °C and $T_{CO_2,cond} = 3.67$ °C, respectively. The discharged energy over the cycle is further enhanced
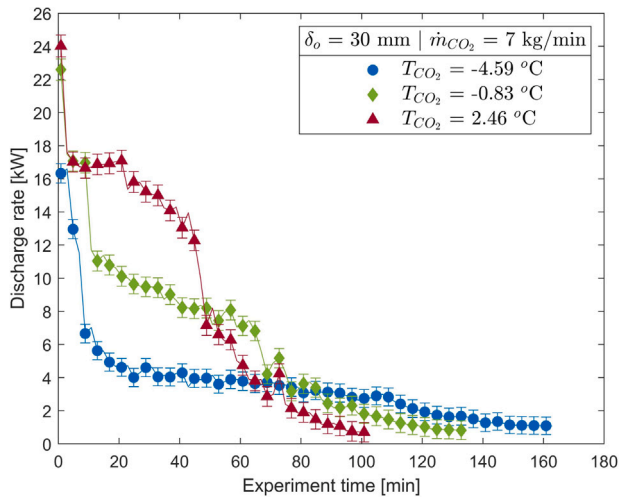
Fig. 13. Discharging rates for various refrigerant condensation temperatures ($T_{CO_2,cond}$ = −4.59 °C, $T_{CO_2,cond}$ = −0.88 °C and $T_{CO_2,cond}$ = 2.46 °C) for $\dot{m}_{CO_2}$ = 7 kg/min and a δ_o = 30 mm.
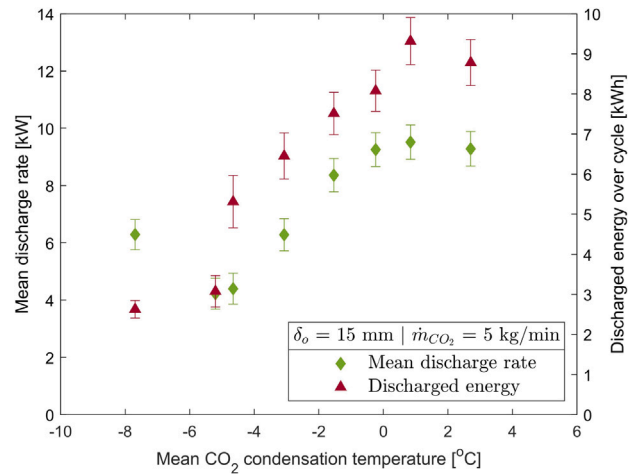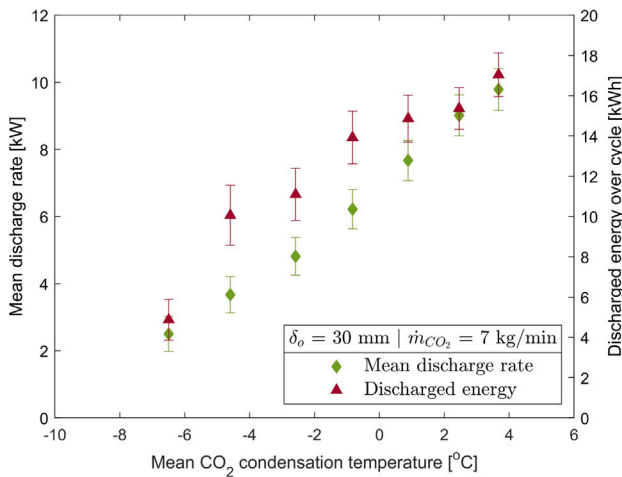

Fig. 14. Mean discharging rate and discharged energy as a function of the refrigerant condensation temperature using a refrigerant mass flow rate of $\dot{m}_{CO_2}$ = 7 kg/min and plate pitch δ_o = 30 mm.

by sensible heat when the phase change process is completed: for higher $T_{CO_2,cond}$, the final PCM temperature reached at the end of the process are also higher towards the refrigerant temperature. For a condensation temperature of −0.8 °C, the theoretical sensible heat discharged over the cycle was calculated to about 7% of the total theoretical discharged energy (latent heat + sensible heat) when considering the volume of PCM between the PPs in the PP-HEX.

The same experiments were reproduced for pitch plate δ_o = 15 mm as for δ_o = 30 mm, using $T_{CO_2,cond}$ = −1 °C to determine the appropriate refrigerant mass flow rate that results in the best performance of the cycle. It was found that the refrigerant mass flow rate of $\dot{m}_{CO_2}$ = 5 kg/min provided the highest amount of discharged energy (kWh) and thus selected for the rest of the test campaign. The mean discharging rate and the discharged energy over the cycle by variation of the refrigerant condensation temperature from $T_{CO_2,cond}$ = −7.70 °C to $T_{CO_2,cond}$ = 2.71 °C are presented in Fig. 15. The same observations can be made as for the δ_o = 30 mm configuration, both the discharged energy over the cycle and the mean discharging rate increases as the condensation temperature of the refrigerant increases. The maximum discharged energy (9.32 kWh) and mean discharge rate (kW) were obtained using $T_{CO_2,cond}$ = 0.84 °C. It was found that a $T_{CO_2,cond}$ higher

Fig. 15. Mean discharging rate and discharged energy as a function of the refrigerant condensation temperature using a refrigerant mass flow rate of $\dot{m}_{CO_2}$ = 5 kg/min and plate pitch δ_o = 15 mm.

than −4.65 °C is required to ensure the entire melting of the solid PCM fraction by the end of the discharging cycle, compared to $T_{CO_2,cond}$ = −2.58 °C for the δ_o = 30 mm configuration. This shows that the discharging process for the δ_o = 15 mm configuration can be operated effectively with approximately 2 K lower difference in $T_{CO_2,cond}$ and $T_{PCM,pc}$ compared to the δ_o = 30 mm due to the shorter plate pitch. For the lowest $T_{CO_2,cond}$ (−7.70 °C), the temperature difference between the $T_{CO_2,cond}$ and $T_{PCM,pc}$ was not sufficient to sustain the discharging cycle and ended after the initial period of the cycle (where the discharge rate is high, see Fig. 15).

Table 6 presents a summary of the discharging performance of the CTES unit for both δ_o = 15 mm and δ_o = 30 mm plate configurations. Three tests using different CO_2 condensation temperatures are selected to represent the performance of the whole temperature range. For δ_o = 15 mm, a 90% increase in the mean discharging rate and 41% increase in the discharged energy over the cycle are obtained when increasing the difference between the $T_{CO_2,cond}$ and $T_{PCM,pc}$ by 63% (from 4.95 K to 8.07 K). A further increase of the condensation temperature by 2.37 K to $T_{CO_2,cond}$ = 0.84 °C results in just a 14% and 24% increase in the discharge rate and discharged energy, respectively. In summary, the relatively small plate pitch of 15 mm allows for an efficient discharging process of the CTES unit by using a temperature difference between the melting point of the PCM and condensing refrigerant of about 8 K. It is concluded that the CTES design consisting of δ_o = 15 mm using $\dot{m}_{CO_2}$ = 5 kg/min and $T_{CO_2,cond}$ = −1.53 °C is appropriate to ensure peak shaving of the refrigeration load in a refrigeration process characterised by load peaks which last ≈ 1 h. For the 30 mm plate pitch, the increase in the discharging rate and discharged energy over the cycle has a more linear profile than that for the 15 mm plate pitch. This behaviour is expected as the increased distance between the PPs results in more thermal resistance to the heat transfer process as the discharging cycle progresses. Consequently, the discharging performance of the CTES unit is more sensitive to higher $T_{CO_2,cond}$ when using δ_o = 30 mm compared to δ_o = 15 mm. When the condensation temperature is increased from −4.59 °C to −0.83 °C (3.76 K), an increase of 67% in the mean discharge rate and an increase of 38% in the discharged energy over the cycle is observed. A further increase in the $T_{CO_2,cond}$ by 4.5 K (from −0.83 °C to 3.67 °C) results in a 57% and 22% increase in the discharging rate and discharged energy, respectively. The discharging time (t_D) was found to be more influenced by the $T_{CO_2,cond}$ for the δ_o = 30 mm configuration than for δ_o = 15 mm. For δ_o = 30 mm, t_D is reduced by ≈ 30 min when increasing $T_{CO_2,cond}$ from −4.59 °C to −0.83 °C and further reduced by ≈ 30 min when increasing $T_{CO_2,cond}$ from −0.83 °C to 3.67 °C.

Table 6
Summary of the discharging performance for the CTES unit for various CO_2 condensation temperature for a plate pitch of 15 mm and 30 mm.

δ_o [mm]	$\dot{m}_{CO_2}$ [kg/min]	T_c [°C]	$\dot{E}_r$ [kW]	E_D [kWh]	t_D [min]
15	5.0	−4.65	4.40 ± 0.540	5.31 ± 0.653	73
15	5.0	−1.53	8.36 ± 0.583	7.51 ± 0.523	54
15	5.0	0.84	9.52 ± 0.601	9.32 ± 0.589	59
30	7.0	−4.59	3.67 ± 0.542	10.06 ± 1.49	165
30	7.0	−0.83	6.22 ± 0.584	13.92 ± 1.31	135
30	7.0	3.67	9.79 ± 0.625	17.04 ± 1.09	105

The results for the discharging process summarised in Table 6 can be used as a design guide to engineer similar CTES units to be implemented in the industry. The results from the discharging process have demonstrated that peak shifting of the refrigeration demand is feasible when integrating this novel CTES unit into a CO_2 refrigeration system. The flexible design of the CTES unit allows the designer to select a discharge characteristic of the CTES unit that matches the refrigeration load curve in different refrigeration systems. It was found that the 15 mm plate pitch is the appropriate choice to reduce load peak with high magnitude and a duration of approximately one hour. On the other hand, it was found that the 30 mm plate pitch is most suitable when the peak has a longer duration and a lower magnitude. However, it is possible to install several of these CTES units in parallel to increase the overall energy storage capacity or increase the total discharge rate of the CTES system.

7. Conclusions

This paper presents the design and thorough experimental performance testing of a CTES unit based on a pillow plate heat exchanger with a low-temperature commercial PCM as the storage medium. It is one of the first experimental investigations to couple the phase change process of a subzero PCM (solidification/melting) with the phase change process of the refrigerant (evaporation/condensation) in the same heat exchanger. The results from the experimental testing have demonstrated the feasibility of using the CTES unit with PCM for peak shifting of the refrigeration load. The main findings can be summarised as follows:

- The charging time of the CTES unit was mainly affected by reducing the CO_2 evaporation temperature, effectively increasing the temperature difference between the CO_2 refrigerant and the phase change temperature of the PCM. Decreasing the $T_{CO_2,evap}$ from −13 °C to −15.5 °C yielded a reduction in the charging time by 44% for $\delta_o = 30$ mm.
- The discharging rate was found to be generally high during the initial phase of the cycle and continually decreasing towards the end of the cycle, and was mainly affected by increasing the $T_{CO_2,cond}$. The maximum discharged energy was found to be 17.04 kWh using $\delta_o = 30$ mm with $T_{CO_2,cond} = 3.67$ °C, yielding a mean discharge rate of 9.79 kW.
- The flexible design of the CTES unit allows the designer to select a discharge characteristic of the CTES unit that matches the refrigeration load curve of the refrigeration plant by changing the plate pitch. A plate pitch of $\delta_o = 15$ mm was found as the appropriate choice to reduce a peak with a high magnitude and duration of approximately one hour, while $\delta_o = 30$ mm is most suitable for peaks of about 2 h with a lower magnitude.

The demonstrated module-based CTES technology is versatile and is expected to be scaleable for implementation in industrial refrigeration plants with various temperature requirements and load characteristics. The planned future studies on the technology are the development and validation of a dynamic numerical model to investigate the impact of integrating CTES technology into a complete refrigeration plant. Furthermore, it is relevant to investigate any performance degradation of the CTES unit over time, as well as partial charging and discharging cycles.

Declaration of competing interest

The authors declare that they have no known competing financial interests or personal relationships that could have appeared to influence the work reported in this paper.

References

[1] A. Arteconi, F. Polonara, Demand side management in refrigeration applications, Int. J. Heat Technol. 35 (1) (2017) 58–63.

[2] P. Moreno, C. Solé, A. Castell, L.F. Cabeza, The use of phase change materials in domestic heat pump and air-conditioning systems for short term storage: A review, Renew. Sustain. Energy Rev. 39 (2014) 1–13.

[3] M.M. Joybari, F. Haghighat, J. Moffat, P. Sra, Heat and cold storage using phase change materials in domestic refrigeration systems: The state-of-the-art review, Energy Build. 106 (2015) 111–124.

[4] H. Selvnes, Y. Allouche, R.I. Manescu, A. Hafner, Review on cold thermal energy storage applied to refrigeration systems using phase change materials, Therm. Sci. Eng. Prog. 22 (2021) 100807.

[5] P. Gullo, A. Hafner, K. Banasiak, Transcritical R744 refrigeration systems for supermarket applications: Current status and future perspectives, Int. J. Refrig. 93 (2018) 269–310.

[6] G. Li, Y. Hwang, R. Radermacher, H.-H. Chun, Review of cold storage materials for subzero applications, Energy 51 (2013) 1–17.

[7] Y. Allouche, S. Varga, C. Bouden, A.C. Oliveira, Experimental determination of the heat transfer and cold storage characteristics of a microencapsulated phase change material in a horizontal tank, Energy Convers. Manage. 94 (2015) 275–285.

[8] A. Abhat, Low temperature latent heat thermal energy storage: heat storage materials, Sol. Energy 30 (4) (1983) 313–332.

[9] E. Oró, A. De Gracia, A. Castell, M.M. Farid, L.F. Cabeza, Review on phase change materials (PCMs) for cold thermal energy storage applications, Appl. Energy 99 (2012) 513–533.

[10] A. Safari, R. Saidur, F. Sulaiman, Y. Xu, J. Dong, A review on supercooling of phase change materials in thermal energy storage systems, Renew. Sustain. Energy Rev. 70 (2017) 905–919.

[11] Y.J. Zhou, E.J. Kerkhoven, J. Nielsen, Barriers and opportunities in bio-based production of hydrocarbons, Nat. Energy 3 (11) (2018) 925–935.

[12] PureTemp LCC, PureTemp phase change materials, 2020, URL: https://www.puretemp.com/stories/puretemp-safety-data-sheets.

[13] Croda International Plc, CrodaTherm phase change materials, 2020, URL: https://www.crodaenergytechnologies.com/en-gb/applications/thermal-energy-storage.

[14] O. Okogeri, V.N. Stathopoulos, What about greener phase change materials? A review on biobased phase change materials for thermal energy storage applications, Int. J. Thermofluids 10 (2021) 100081.

[15] B. Zalba, J.M. Marın, L.F. Cabeza, H. Mehling, Review on thermal energy storage with phase change: materials, heat transfer analysis and applications, Appl. Therm. Eng. 23 (3) (2003) 251–283.

[16] L. Liu, D. Su, Y. Tang, G. Fang, Thermal conductivity enhancement of phase change materials for thermal energy storage: A review, Renew. Sustain. Energy Rev. 62 (2016) 305–317.

[17] S. Wu, T. Yan, Z. Kuai, W. Pan, Thermal conductivity enhancement on phase change materials for thermal energy storage: A review, Energy Storage Mater. 25 (2020) 251–295.

[18] EU, Directive 2014/68/EU of the European Parliament and of the Council of 15 May 2014 on the harmonisation of the laws of the Member States relating to the making available on the market of pressure equipmen, Off. J. Eur. Union (2014).

[19] T. Korth, F. Loistl, C. Schweigler, Novel integration of latent heat storage in multi-split air conditioning systems, in: 25th IIR International Congress of Refrigeration Proceedings, International Institute of Refrigeration, 2019.

[20] M.A. Ezan, A. Erek, I. Dincer, Energy and exergy analyses of an ice-on-coil thermal energy storage system, Energy 36 (11) (2011) 6375–6386.

[21] N. Tay, M. Belusko, F. Bruno, Experimental investigation of tubes in a phase change thermal energy storage system, Appl. Energy 90 (1) (2012) 288–297.

[22] A. López-Navarro, J. Biosca-Taronger, B. Torregrosa-Jaime, J. Corberán, J. Bote-García, J. Payá, Experimental investigations on the influence of ice floating in an internal melt ice-on-coil tank, Energy Build. 57 (2013) 20–25.

[23] A. López-Navarro, J. Biosca-Taronger, B. Torregrosa-Jaime, I. Martínez-Galván, J.M. Corberán, J. Esteban-Matías, J. Paya, Experimental investigation of the temperatures and performance of a commercial ice-storage tank, Int. J. Refrig. 36 (4) (2013) 1310–1318.

[24] A. Abhishek, B. Kumar, M.H. Kim, Y.T. Lee, J.D. Chung, S.T. Kim, T. Kim, C. Lee, K. Lee, Comparison of the performance of ice-on-coil LTES tanks with horizontal and vertical tubes, Energy Build. 183 (2019) 45–53.

[25] H. Selvnes, V. Büttner, A. Hafner, Evaluation of a pillow-plate heat exchanger for a pump-circulated CO2 refrigeration system, in: Proceedings of the 14th IIR-Gustav Lorentzen Conference on Natural Refrigerants, International Institute of Refrigeration, 2020.

[26] H. Selvnes, Y. Allouche, A. Hafner, Experimental characterisation of a cold thermal energy storage unit with a pillow-plate heat exchanger design, Appl. Therm. Eng. (2021) 117507.

[27] A. Castell, M. Belusko, F. Bruno, L.F. Cabeza, Maximisation of heat transfer in a coil in tank PCM cold storage system, Appl. Energy 88 (11) (2011) 4120–4127.

[28] B. Torregrosa-Jaime, A. López-Navarro, J.M. Corberán, J. Esteban-Matías, L. Klinkner, J. Payá, Experimental analysis of a paraffin-based cold storage tank, Int. J. Refrig. 36 (6) (2013) 1632–1640.

[29] A. López-Navarro, J. Biosca-Taronger, J. Corberán, C. Peñalosa, A. Lázaro, P. Dolado, J. Payá, Performance characterization of a PCM storage tank, Appl. Energy 119 (2014) 151–162.

[30] F. Bosholm, A. López-Navarro, M. Gamarra, J. Corberán, J. Payá, Reproducibility of solidification and melting processes in a latent heat thermal storage tank, Int. J. Refrig. 62 (2016) 85–96.

[31] M. Qu, Y. Tang, T. Zhang, Z. Li, J. Chen, Experimental investigation on the multi-mode heat discharge process of a PCM heat exchanger during TES based reverse cycle defrosting using in cascade air source heat pumps, Appl. Therm. Eng. 151 (2019) 154–162.

[32] R.M. Saeed, J.P. Schlegel, R. Sawafta, V. Kalra, Plate type heat exchanger for thermal energy storage and load shifting using phase change material, Energy Convers. Manage. 181 (2019) 120–132.

[33] T. Korth, F. Loistl, A. Storch, R. Schex, A. Krönauer, C. Schweigler, Capacity enhancement of air conditioning systems by direct integration of a latent heat storage unit, Appl. Therm. Eng. 167 (2020) 114727.

[34] Calmac Corp., Thermal energy storage in supermarkets, 2015, URL: http://www.calmac.com/stuff/contentmgr/files/0/a2c6d5b156fea7639cd0cd619f36c95a/pdf/ib_155_supermarket_market_brochure_160811.pdf.

[35] Viessmann Refrigeration Solutions, ESyCool green - Sustainable energy systems for food retailing, 2018, URL: https://cooling.viessmann.co.uk/en-gb/our-products/esycool-green.

[36] B. Ballot-Miguet, G. Dejardins, B. Quaro, A. Defruit, D. Rousset, Increasing the performances of a CO2 refrigeration system using cool thermal energy storage for subcooling: a supermarket application, in: Proceedings of the 25th IIR International Congress of Refrigeration, 2019, pp. 1062–1069.

[37] E.H. Verpe, I. Tolstorebrov, A. Sevault, A. Hafner, Y. Ladam, Cold thermal energy storage with low-temperature plate freezing of fish on offshore vessels, in: Proceedings of the 25th IIR International Congress of Refrigeration. Montréal, Canada, August 24-30, 2019, IIR, 2019.

[38] H. Selvnes, A. Hafner, H. Kauko, Design of a cold thermal energy storage unit for industrial applications using CO2 as refrigerant, in: 25th IIR International Congress of Refrigeration Proceedings, IIR, 2019.

[39] S. James, C. James, The food cold-chain and climate change, Food Res. Int. 43 (7) (2010) 1944–1956.

[40] D. Coulomb, Refrigeration and cold chain serving the global food industry and creating a better future: two key IIR challenges for improved health and environment, Trends Food Sci. Technol. 19 (8) (2008) 413–417.

[41] E. Oró, L. Miró, C. Barreneche, I. Martorell, M.M. Farid, L.F. Cabeza, Corrosion of metal and polymer containers for use in PCM cold storage, Appl. Energy 109 (2013) 449–453.

[42] M. Piper, A. Olenberg, J. Tran, E. Kenig, Determination of the geometric design parameters of pillow-plate heat exchangers, Appl. Therm. Eng. 91 (2015) 1168–1175.

[43] J. Tran, S. Sommerfeld, M. Piper, E. Kenig, Investigation of pillow-plate condensers for the application in distillation columns, Chem. Eng. Res. Des. 99 (2015) 67–74.

[44] M. Piper, A. Zibart, J. Tran, E. Kenig, Numerical investigation of turbulent forced convection heat transfer in pillow plates, Int. J. Heat Mass Transfer 94 (2016) 516–527.

[45] M. Piper, A. Zibart, E. Kenig, New design equations for turbulent forced convection heat transfer and pressure loss in pillow-plate channels, Int. J. Therm. Sci. 120 (2017) 459–468.

[46] M. Shirzad, M.A. Delavar, S.S.M. Ajarostaghi, K. Sedighi, Evaluation the effects of geometrical parameters on the performance of pillow plate heat exchanger, Chem. Eng. Res. Des. 150 (2019) 74–83.

[47] S. Kumar, B. Premachandran, P. Subbarao, Study on thermo–hydraulics in a pillow plate channel, Int. J. Therm. Sci. 145 (2019) 106020.

[48] C. Elliott, V. Vijayakumar, W. Zink, R. Hansen, National instruments LabVIEW: a programming environment for laboratory automation and measurement, JALA: J. Assoc. Lab. Autom. 12 (1) (2007) 17–24.

[49] HERMETIC Pumpen GmbH, HERMETIC refrigeration pumps, 2021, URL: https://kaelte.hermetic-pumpen.com/en/pump-types.

[50] DOW Chemical Company, DOWCAL 100 heat transfer fluid technical data sheet, 2021, URL: https://www.dow.com/en-us/document-viewer.html?ramdomVar=5550034686195609151&docPath=/content/dam/dcc/documents/en-us/productdatasheet/180/180-01588-01-dowcal-100-heat-transfer-fluid-tds.pdf.

[51] E. Lemmon, I. Bell, M. Huberm, M. McLinden, NIST Standard Reference Database 23: Reference Fluid Thermodynamic and Transport Properties-REFPROP, Version 10.0, National Institute of Standards and Technology, 2018, URL: https://www.nist.gov/srd/refprop.

[52] IEC ISO and BIPM OIML, Guide to the Expression of Uncertainty in Measurement, Vol. 122, Geneva, Switzerland, 1995, pp. 16–17.

[53] Rubitherm Technologies GmbH, Data sheet RT-9HC, 2020, URL: https://www.rubitherm.eu/media/products/datasheets/Techdata_-RT-9HC_EN_29092020.PDF.

[54] German Institute for quality assurance and certification, Phase change materials, quality assurance RAL-GZ 896, 2018, URL: https://www.pcm-ral.org/pdf/RAL_GZ_896_Phase_Change_Material_Edition_March_2018.pdf.

[55] C. Barreneche, A. Solé, L. Miró, I. Martorell, A.I. Fernández, L.F. Cabeza, Study on differential scanning calorimetry analysis with two operation modes and organic and inorganic phase change material (PCM), Thermochim. Acta 553 (2013) 23–26.

[56] S. Gschwander, T. Haussmann, G. Hagelstein, C. Barreneche, G. Ferrer, L. Cabeza, G. Diarce, W. Hohenauer, D. Lager, C. Rathgeber, et al., Standardization of PCM characterization via DSC, in: Proceedings of SHC 2015 International Conference on Solar Heating and Cooling for Buildings and Industry, 2015, pp. 2–4.

[57] G. Feng, K. Huang, H. Xie, H. Li, X. Liu, S. Liu, C. Cao, DSC test error of phase change material (PCM) and its influence on the simulation of the PCM floor, Renew. Energy 87 (2016) 1148–1153.

[58] M.N. Sam, A. Caggiano, C. Mankel, E. Koenders, A comparative study on the thermal energy storage performance of bio-based and paraffin-based PCMs using DSC procedures, Materials 13 (7) (2020) 1705.

[59] K.-H. Breuer, W. Eysel, The calorimetric calibration of differential scanning calorimetry cells, Thermochim. Acta 57 (3) (1982) 317–329.

[60] TA Instruments, Enthalpy of melting for standards, 2021, URL: https://www.tainstruments.com/pdf/literature/TN11.pdf.

[61] Y. Liu, X. Li, P. Hu, G. Hu, Study on the supercooling degree and nucleation behavior of water-based graphene oxide nanofluids PCM, Int. J. Refrig. 50 (2015) 80–86.

[62] S.E. Gustafsson, Transient plane source techniques for thermal conductivity and thermal diffusivity measurements of solid materials, Rev. Sci. Instrum. 62 (3) (1991) 797–804.

[63] J.C. Dixon, The Shock Absorber Handbook, John Wiley & Sons, 2008.

[64] J. Sengers, J.T.R. Watson, Improved international formulations for the viscosity and thermal conductivity of water substance, J. Phys. Chem. Ref. Data 15 (4) (1986) 1291–1314.

[65] A. Tambovtsev, H. Quack, COP improvement by transfer of the superheating into the internal heat exchanger, in: International Congress of Refrigeration, Beijing, China, 2007.

[66] S. Minetto, R. Brignoli, C. Zilio, S. Marinetti, Experimental analysis of a new method for overfeeding multiple evaporators in refrigeration systems, Int. J. Refrig. 38 (2014) 1–9.

[67] S. Bortolin, M. Rossato, S. Bernardinello, D. Del Col, Investigation of evaporator performance with and without liquid overfeeding, in: International Refrigeration and Air Conditioning Conference, Purdue, US, 2016.

[68] G. Mitsopoulos, E. Syngounas, D. Tsimpoukis, E. Bellos, C. Tzivanidis, S. Anagnostatos, Annual performance of a supermarket refrigeration system using different configurations with CO2 refrigerant, Energy Convers. Manage.: X 1 (2019) 100006.

[69] O. Arsenyeva, J. Tran, M. Piper, E. Kenig, An approach for pillow plate heat exchangers design for single-phase applications, Appl. Therm. Eng. 147 (2019) 579–591.